

## Article

# Exploring the Remarkably High Photocatalytic Efficiency of Ultra-Thin Porous Graphitic Carbon Nitride Nanosheets

Zahra Kalantari Bolaghi, Cristina Rodriguez-Seco \*, Aycan Yurtsever and Dongling Ma \* 

Centre Énergie Matériaux et Télécommunications, Institut National de la Recherche Scientifique (INRS), Varennes, QC J3X 1P7, Canada; zahra.kalantari@inrs.ca (Z.K.B.); aycan.yurtsever@inrs.ca (A.Y.)

\* Correspondence: cristina.rodriguez.seco@inrs.ca (C.R.-S.); dongling.ma@inrs.ca (D.M.)

**Abstract:** Graphitic carbon nitride (g-C<sub>3</sub>N<sub>4</sub>) is a metal-free photocatalyst used for visible-driven hydrogen production, CO<sub>2</sub> reduction, and organic pollutant degradation. In addition to the most attractive feature of visible photoactivity, its other benefits include thermal and photochemical stability, cost-effectiveness, and simple and easy-scale-up synthesis. However, its performance is still limited due to its low absorption at longer wavelengths in the visible range, and high charge recombination. In addition, the exfoliated nanosheets easily aggregate, causing the reduction in specific surface area, and thus its photoactivity. Herein, we propose the use of ultra-thin porous g-C<sub>3</sub>N<sub>4</sub> nanosheets to overcome these limitations and improve its photocatalytic performance. Through the optimization of a novel multi-step synthetic protocol, based on an initial thermal treatment, the use of nitric acid (HNO<sub>3</sub>), and an ultrasonication step, we were able to obtain very thin and well-tuned material that yielded exceptional photodegradation performance of methyl orange (MO) under visible light irradiation, without the need for any co-catalyst. About 96% of MO was degraded in as short as 30 min, achieving a normalized apparent reaction rate constant (*k*) of  $1.1 \times 10^{-2} \text{ min}^{-1} \text{ mg}^{-1}$ . This represents the highest *k* value ever reported using C<sub>3</sub>N<sub>4</sub>-based photocatalysts for MO degradation, based on our thorough literature search. Ultrasonication in acid not only prevents agglomeration of g-C<sub>3</sub>N<sub>4</sub> nanosheets but also tunes pore size distribution and plays a key role in this achievement. We also studied their performance in a photocatalytic hydrogen evolution reaction (HER), achieving a production of 1842  $\mu\text{mol h}^{-1} \text{ g}^{-1}$ . Through a profound analysis of all the samples' structure, morphology, and optical properties, we provide physical insight into the improved performance of our optimized porous g-C<sub>3</sub>N<sub>4</sub> sample for both photocatalytic reactions. This research may serve as a guide for improving the photocatalytic activity of porous two-dimensional (2D) semiconductors under visible light irradiation.

**Keywords:** photodegradation; hydrogen evolution reaction; porous carbon nitride; exfoliation



**Citation:** Kalantari Bolaghi, Z.; Rodriguez-Seco, C.; Yurtsever, A.; Ma, D. Exploring the Remarkably High Photocatalytic Efficiency of Ultra-Thin Porous Graphitic Carbon Nitride Nanosheets. *Nanomaterials* **2024**, *14*, 103. <https://doi.org/10.3390/nano14010103>

Academic Editor: Peter Kasak

Received: 30 November 2023

Revised: 29 December 2023

Accepted: 29 December 2023

Published: 1 January 2024



**Copyright:** © 2024 by the authors. Licensee MDPI, Basel, Switzerland. This article is an open access article distributed under the terms and conditions of the Creative Commons Attribution (CC BY) license (<https://creativecommons.org/licenses/by/4.0/>).

## 1. Introduction

The exponential rise in urban populations, rapid economic progress, and long-term industrial and agricultural activities have caused a severe energy crisis and produced harmful pollutants that led to climate change. This is having a tremendous negative effect on both human health and the environment [1–3]. Specifically, the discharge of waste materials, such as organic dyes, surfactants, chloro-organic compounds, or pesticides, from certain industries became a significant threat to public health, aquatic life, and ecosystems. The main causes include their toxic nature, persistence in the environment, and their ability to alter natural habitat balance and harm numerous living organisms [4–6]. Furthermore, the increased global utilization of fossil fuels in the past decades is directly related to human economic and social development. However, it is provoking a severe energy crisis, additional pollution, and an acceleration of global warming. To tackle above-mentioned problems, we need to seek more environmentally friendly technologies that lower the energy requirements and production costs [7–9].

To date, several traditional methods have been utilized, including adsorption [10], filtration [11], and electrochemical processes [12]. However, they fall short in completely getting rid of organic pollutants and require high energy consumption and cost [13]. Solar-involved photocatalysis stands out as a highly efficient technology that converts abundant solar energy into chemical energy in the presence of a semiconductor catalyst. It can be used for various applications, including hydrogen production [14,15], CO<sub>2</sub> reduction [16,17], N<sub>2</sub> fixation [18,19], and water purification [20,21], among others. Compared to previously mentioned methods, photocatalysis has lower energy and operating costs, is more sustainable, and requires minimal use of chemicals [22]. Additionally, the materials used in this process are more stable, reducing the need for frequent replacement [23,24]. In a photocatalytic reaction, electron–hole pairs are generated in a semiconductor upon illumination. These electrons and holes migrate to the photocatalyst surface to take part in redox reactions. Numerous semiconductors, including TiO<sub>2</sub> [25], ZnS [26], ZnO [27], CdS [28], and Cu<sub>2</sub>O [29], have been widely used in the past few decades for pollutant degradation and hydrogen production. However, their photocatalytic efficiency is low, limiting their practical application. This is due to their wide bandgap, which decreased photo-response range and visible light-harvesting capabilities, and fast photoinduced charge carrier recombination [30–32]. Thus, it is imperative to seek out new strategies and alternative materials that allow us to efficiently utilize solar energy and improve photocatalytic activity.

Carbon nitride (C<sub>3</sub>N<sub>4</sub>) has gained significant interest as a photocatalyst in the field of pollutant degradation and hydrogen production due to its visible photoactivity and other outstanding properties [33–36]. C<sub>3</sub>N<sub>4</sub> is a metal-free semiconductor that possesses visible absorption, has a layered structure, shows great thermal and chemical stability, and features low-cost and easy synthesis [37–39]. Its band gap (2.7 eV) and valence and conduction band edges (1.3 eV and −1.4 eV versus standard hydrogen electrode (NHE), respectively) make it suitable for water splitting, degradation of organic pollutants, and CO<sub>2</sub> reduction [40,41]. However, its practical applications are hindered because of its still limited absorption in the visible range, a high recombination rate of photogenerated charge carriers, and a low specific surface area caused by its bulk nature [42–44]. To address its shortcomings, numerous efforts have been made, including metal and non-metal doping [45], defect engineering [46], surface modification with other carbon-based nanomaterials [47], morphology modulation [48], and coupling with other lower-bandgap semiconductors [49]. Nevertheless, improving the photocatalytic performance of C<sub>3</sub>N<sub>4</sub>-based materials to a suitable level, without involving any expensive metals, has remained a significant challenge [50,51].

The two-dimensional (2D) nanosheet structure enhances the photocatalytic activity of g-C<sub>3</sub>N<sub>4</sub>, with respect to its bulk counterpart, by significantly improving its light absorption and increasing its surface area [52,53]. Further reducing the thickness of the nanosheets to make ultra-thin materials with few layers, typically below 10 nm in thickness, can further reduce charge carrier diffusion length, boost its light absorption, lower the recombination rate, and provide more exposed active sites for closer interface contact between the photocatalyst and pollutants [54,55]. Additionally, ultra-thin materials can be further modified by attaching functional groups onto their surface to fine-tune their electronic, optical, and chemical properties [39]. A useful technique for separating stacked layers of g-C<sub>3</sub>N<sub>4</sub> into thinner ones is through exfoliation, such as ball milling, and chemical, ultrasonication, and thermal treatments [56,57]. The process of chemical exfoliation usually involves the use of oxidizing acids such as nitric acid (HNO<sub>3</sub>) and sulfuric acid (H<sub>2</sub>SO<sub>4</sub>) [58,59]. During this process, H<sup>+</sup> intercalates between layers of C<sub>3</sub>N<sub>4</sub> using nitrogen as acceptor sites, which causes crystal swelling, increases the interlamellar distance, and decreases sheet attraction [60,61]. As a result, g-C<sub>3</sub>N<sub>4</sub> nanosheets become separated. For example, Xu et al. [62] synthesized ultra-thin g-C<sub>3</sub>N<sub>4</sub> nanosheets using chemical exfoliation with H<sub>2</sub>SO<sub>4</sub>. They obtained single-layered nanosheets with a large surface area and superior transport of photogenerated charge carriers, enhancing their photocatalytic activity by 2.6 times when compared to bulk C<sub>3</sub>N<sub>4</sub>. It has also been demonstrated that the use of HNO<sub>3</sub> during the

chemical exfoliation process introduces N vacancies and increases the possibility that O atoms replace the mentioned vacancies simultaneously. This modifies the density of the photoinduced electrons and holes, the band gap, and the visible light absorption in the photocatalyst [63,64]. Zhang et al. [65] revealed that the introduction of cyano groups and N vacancies into porous  $C_3N_4$  resulted in 26 times higher hydrogen production compared to bulk  $C_3N_4$ . This was caused by defects that improve charge separation efficiency and promote its light-harvesting capacity. In another study, Niu et al. [66] demonstrated that N vacancies introduced to bulk  $C_3N_4$  can lead to an increase in light absorption between 450 nm and 600 nm and a narrowing of the band gap from 2.74 eV to 2.66 eV. Ultrasonication in liquid media creates microbubbles and powerful jets, highly increasing pressure and temperature locally. These ultrasonic waves break down the weak van der Waals forces of g- $C_3N_4$  layers, leading to the formation of nanosheets [67,68]. The presence of dangling hydrogens among multilayer  $C_3N_4$  makes polar solvents, such as water, ethanol, and ammonia, more effective for ion intercalation [69]. Zhang et al. [70] used ultrasonication to exfoliate bulk  $C_3N_4$  in water, yielding thin sheets of 70–160 nm in size and 2.5 nm in height (equivalent to seven layers of C-N). These sheets showed enhanced photo-absorption that translated into an increased photocurrent and a three times higher photocatalytic activity when compared to bulk  $C_3N_4$ , for Rhodamine B (RhB) photodegradation in the presence of  $H_2O_2$ .

In addition, the incorporation of pores into g- $C_3N_4$  nanosheets is expected to increase specific surface area, surface active sites, and charge separation [71,72]. Altering the pore configuration and size distribution of porous g- $C_3N_4$  nanosheets is a successful approach for enhancing its optoelectronic properties and photocatalytic efficacy [73]. For example, Zhang et al. [74] synthesized mesoporous g- $C_3N_4$  using HCl and ethanol, and obtained higher specific area and pore volume that yielded a greater activity for the degradation of RhB (degradation percentage of 99.9% in 210 min) compared to that of g- $C_3N_4$  (degradation percentage of 61.4% in 240 min).

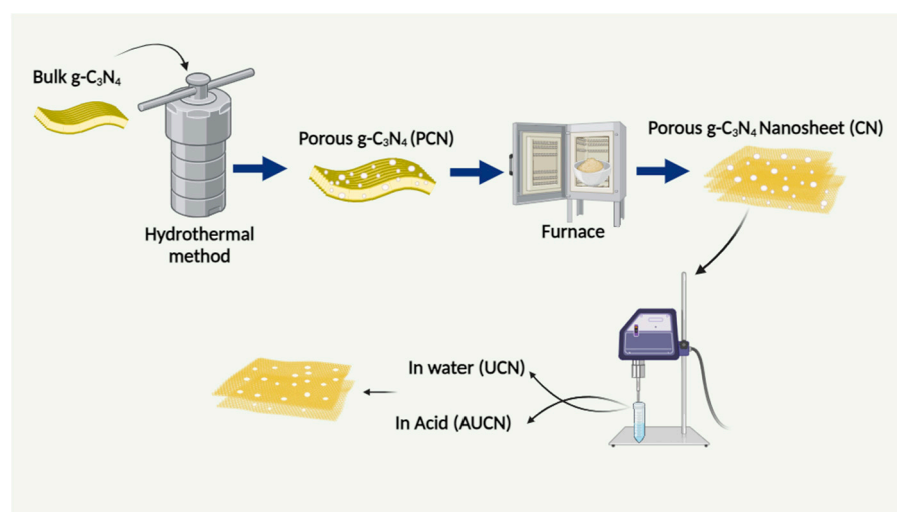
In this study, we synthesized ultra-thin porous g- $C_3N_4$  nanosheets, by means of thermal exfoliation and ultrasonication in an acid medium. We achieved a substantial time and energy reduction during the exfoliation step using acid when compared to prior publications that required long hours of stirring in acid media, or a high temperature [75–78]. Moreover, the addition of  $HNO_3$  and ultrasonication greatly modified the chemical and physical properties of porous g- $C_3N_4$ -based samples. We present here a rigorous study of how the synthetic steps affect the photocatalytic performance of our materials when used for pollutant degradation and hydrogen production by thoroughly analyzing their light absorption, structure, morphology, and pore size distribution. With that, we were able to achieve a normalized apparent reaction rate constant ( $k$ ) of  $1.1 \times 10^{-2} \text{ min}^{-1} \text{ mg}^{-1}$ , as well as providing physical insights into materials engineering towards achieving high visible-driven photocatalysis performance of a very promising material based on g- $C_3N_4$ .

## 2. Materials and Methods

Melamine ( $C_3H_6N_6$ , 99%), nitric acid ( $HNO_3$ ), 1,4-benzoquinone (BQ), tert-butyl alcohol (t-BuOH), and disodium ethylenediaminetetraacetate ( $Na_2EDTA$ ) and TEOA (10 vol %) were bought from Sigma-Aldrich Corporation (Oakville, ON, CA) and utilized without any additional processing.

g- $C_3N_4$  samples were synthesized by changing several conditions (i.e., temperature, sonication time, sonication solution) until the optimal sample (thermally treated at 500 °C, 5 min ultrasonication in acid) was obtained (Scheme 1). Bulk  $C_3N_4$  (BCN) was first prepared by heating melamine in a muffle furnace by gradually increasing temperature with a heating rate of  $2.5 \text{ °C min}^{-1}$  under air. Upon reaching 550 °C, heating continued for 4 h and then it gradually cooled down to room temperature. The synthesis of g- $C_3N_4$  nanosheets involved a multi-step method, including a hydrothermal treatment that yielded the formation of a porous structure, and different exfoliation steps to finally obtain ultra-thin nanosheets. First, 0.9 g of BCN was added to 60 mL of deionized water and sonicated for 20 min using a

sonication bath. The dispersion was then poured into a 125 mL Teflon-lined stainless-steel autoclave and heated in an oven at 180 °C for 12 h. The mixture was centrifuged and air-dried at 80 °C overnight. The produced powder was named as porous  $g\text{-C}_3\text{N}_4$  (PCN). To form porous nanosheets, the as-prepared PCN sample (0.5 g) was put in a crucible and heated up in a furnace at a heating rate of 5 °C  $\text{min}^{-1}$  in air and then thermally treated at different temperatures (500 °C, 550 °C, and 600 °C) for 2 h. The corresponding samples were named 500-CN, 550-CN, and 600-CN, respectively. To synthesize ultra-thin porous  $g\text{-C}_3\text{N}_4$  nanosheets, chemical and ultrasonic exfoliation were further used. The as-prepared samples (0.1 g of 500-CN, 550-CN, and 600-CN) were added to 20 mL of diluted  $\text{HNO}_3$  (~8 M). Then, they were sonicated using tip sonication for 5 min. Finally, the samples were washed with water and ethanol to remove potential alkaline residues. Some samples were synthesized via ultrasonic exfoliation only in water for 5 min (500-UCN, 550-UCN, and 600-UCN), and others, as mentioned earlier, via ultrasonic exfoliation for 5 min in the presence of  $\text{HNO}_3$  (500-AUCN, 550-AUCN, and 600-AUCN). A summary of all the prepared samples is shown in Table 1.



**Scheme 1.** Schematic diagram of the synthetic procedure of ultra-thin porous  $g\text{-C}_3\text{N}_4$  nanosheets.

**Table 1.** Typical samples synthesized during the optimization process.

Sample	Hydrothermal Method	Thermal Exfoliation	Ultrasonication in Acid	Ultrasonication in Water
500-CN	180 °C	500 °C	☒	☒
550-CN	180 °C	550 °C	☒	☒
600-CN	180 °C	600 °C	☒	☒
500-UCN	180 °C	500 °C	☒	☑
550-UCN	180 °C	550 °C	☒	☑
600-UCN	180 °C	600 °C	☒	☑
500-AUCN	180 °C	500 °C	☑	☒
550-AUCN	180 °C	550 °C	☑	☒
600-AUCN	180 °C	600 °C	☑	☒

An XPS analysis was conducted using a VG Escalab 220i-XL instrument equipped with a twin-anode (Mg/Al) source. To adjust for charging, the binding energies (BEs) were calibrated against the N1s peak at 299 eV. A CHI 660E electrochemical workstation was used for photoelectrochemical (PEC) measurements in a standard three-electrode cell. The counter and reference electrodes were a Pt wire and an Ag/AgCl electrode (3 M KCl), respectively. The working electrode was made on FTO glass and protected by Scotch tape. The electrolyte solution employed was a pre-purged 0.2 M aqueous  $\text{Na}_2\text{SO}_4$  solution (pH = 6.8), with nitrogen purging carried out for 30 min beforehand. A Newport solar

simulator with intensity of  $100 \text{ mW/cm}^2$  was utilized as the light source. Nyquist plots were acquired with a frequency range of 100 mHz to 100 kHz at a bias of 0.4 V. In addition, through the diffuse reflectance spectroscopy (DRS) technique (Perkin Elmer, Lambda 750), the optical characteristics of porous g-C<sub>3</sub>N<sub>4</sub> nanosheets were investigated. The Varian Cary 5000 scan spectrometer was used to measure MO absorbance in an aqueous solution. A PANalytical X'Pert MRD instrument was employed to evaluate the crystal structures of all samples. A Cu K $\alpha$  radiation source ( $\lambda = 0.15406 \text{ nm}$ ) was used at 45 kV and 40 mA. The Brunauer–Emmett–Teller (BET) instrument model TMAXCN (TMAX-BSD-PM2) was employed to investigate pore size distribution and surface area of porous materials. The photocatalysts' morphology was investigated using a transmission electron microscope (TEM, JEOL 2100F) operating at 200 kV.

The photocatalytic activity of g-C<sub>3</sub>N<sub>4</sub> was evaluated using MO dye, a common contaminant in water, as a model reagent. A typical experiment involved adding 10 mg of the sample into a 100 mL quartz reactor containing a solution of 25 mL of MO (10 mg/L). The mixture was stirred in the absence of light for 30 min to establish an adsorption–desorption equilibrium before being exposed to illumination. A 300 W Xenon lamp positioned 20 cm away from the solution was utilized in this experiment. A long-pass optical filter of 400 nm was used to allow only visible light to pass through. In total, 0.9 mL of MO was sampled throughout various time intervals and centrifuged to separate from the powder. A UV-vis absorption spectrometer was used to determine the absorbance of MO in the supernatant. As our reaction follows the first-order reaction model, the apparent reaction rate constant ( $k_{\text{app}}$ ) was estimated using the equation  $\ln(C_0/C) = k_{\text{app}} t$ , where  $t$  is reaction time, and  $C_0$  and  $C$  are the MO concentrations at time 0 and  $t$ , respectively. The obtained  $k_{\text{app}}$  value was then normalized with the entire mass of the photocatalysts, referred to as the normalized apparent reaction rate constant ( $k$ ) for performance comparison.

To carry out a photocatalytic hydrogen evolution reaction (HER), a top-irradiation Pyrex reaction vessel covered with a quartz glass connected to a closed gas system was used. The process involved dispersing 50 mg of the catalyst in 45 mL of water. In total, 5 mL of TEOA (10 vol %) was added as the sacrificial agent. Platinum (1.0 wt %) was loaded onto the surface of the catalyst through an in situ photo deposition method using H<sub>2</sub>PtCl<sub>6</sub>·6H<sub>2</sub>O as a precursor. To deposit platinum on samples after sonication of the mixture for 5 min, irradiation with a 300 W Xenon lamp, using a full spectrum, was used while stirring for 1 h. Then, the reactor was sealed and vacuumed before being irradiated by a 300 W Xenon lamp for HER. The incident light's wavelength was controlled via an appropriate long-pass cut-off filter ( $\lambda > 400 \text{ nm}$ ). The suspension was continuously stirred and maintained at constant room temperature by circulated cooling water. The evolved gases were analyzed at 60 min time intervals by sampling 1 mL of gas from the reactor and injecting it into a gas chromatograph (GC, 7890B, Agilent Technologies, Mississauga, ON, CA) equipped with a thermal conductivity detector.

### 3. Results and Discussion

In this work, we performed systematic sample optimization by treating bulk g-C<sub>3</sub>N<sub>4</sub> using different conditions and following certain procedures. First, PCN was synthesized from BCN through the hydrothermal treatment, forming a porous structure. Then, for the optimization of the porous samples, thermal exfoliation at various temperatures (500 °C, 550 °C, and 600 °C) was employed as a way to obtain thinner nanosheets. The optimal temperature (500 °C) was selected based on the photocatalytic performance, which was affected by the pore size, functional surface groups, and thin layered structure. Ultimately, we used tip sonication in water and HNO<sub>3</sub> media to obtain ultra-thin-based samples, to introduce defects and functional groups, and increase light absorption. Typical samples involved in the optimization process are listed in Table 1. Numerous characterization tests were carried out to understand how the various conditions affected the structural, morphological, optical, electrical, and photocatalytic properties of final samples.

TEM was performed to analyze the structure and morphology of g-C<sub>3</sub>N<sub>4</sub>. Figure 1 shows typical low and relatively higher magnification TEM images of resulting mesoporous nanosheets exfoliated at 500 °C after ultrasonication in water and acid. It can be observed that sample 500-CN has more layers of g-C<sub>3</sub>N<sub>4</sub> stacked together with larger pore sizes (Figure 1a,b). Similar stacked structures were also observed for 550-CN and 600-CN (Figure S1a,c). After performing sonication (500-UCN), the number of layers decreases, and nanosheets break at the larger pores, creating smaller nanosheets with smaller pores (Figure 1c,d). Upon sonication in HNO<sub>3</sub> (500-AUCN), g-C<sub>3</sub>N<sub>4</sub> displays much smaller pores (~5 nm) and thinner layers due to etching by strong oxidizing acid and ultrasonication together (Figure 1e,f). The nanosheets' breakdown and exfoliation become more noticeable with longer sonication time in an acid medium (Figure S2a,b). Upon comparing Figure 1a,c,e, it becomes evident that ultrasonication in water and acid leads to a notable reduction in the thickness (i.e., the number of layers) of the nanosheets, thereby signifying the successful exfoliation of C<sub>3</sub>N<sub>4</sub>. TEM images for samples exfoliated at 550 °C (550-CN) and 600 °C (600-CN) are shown in Figure S1. The sample treated at 550 °C (Figure S1b) presents a larger pore size than samples exfoliated at 500 °C, possibly decreasing its specific surface area. From Figure S1d, it can be clearly observed that the nanosheets crumbled into small and non-uniform fragments when the thermal treatment temperature increased to 600 °C (sample 600-CN). Also, from its photocatalytic activity, we observed a much lower performance compared to 500-CN and 550-CN. Its poor activity (Table S1) was attributed to its greater pore size and the loss of its nanosheet structure. The photocatalytic performance of 550-CN was also lower than that of 500-CN (Table S1). Therefore, we decided to focus our study on samples treated at 500 °C.

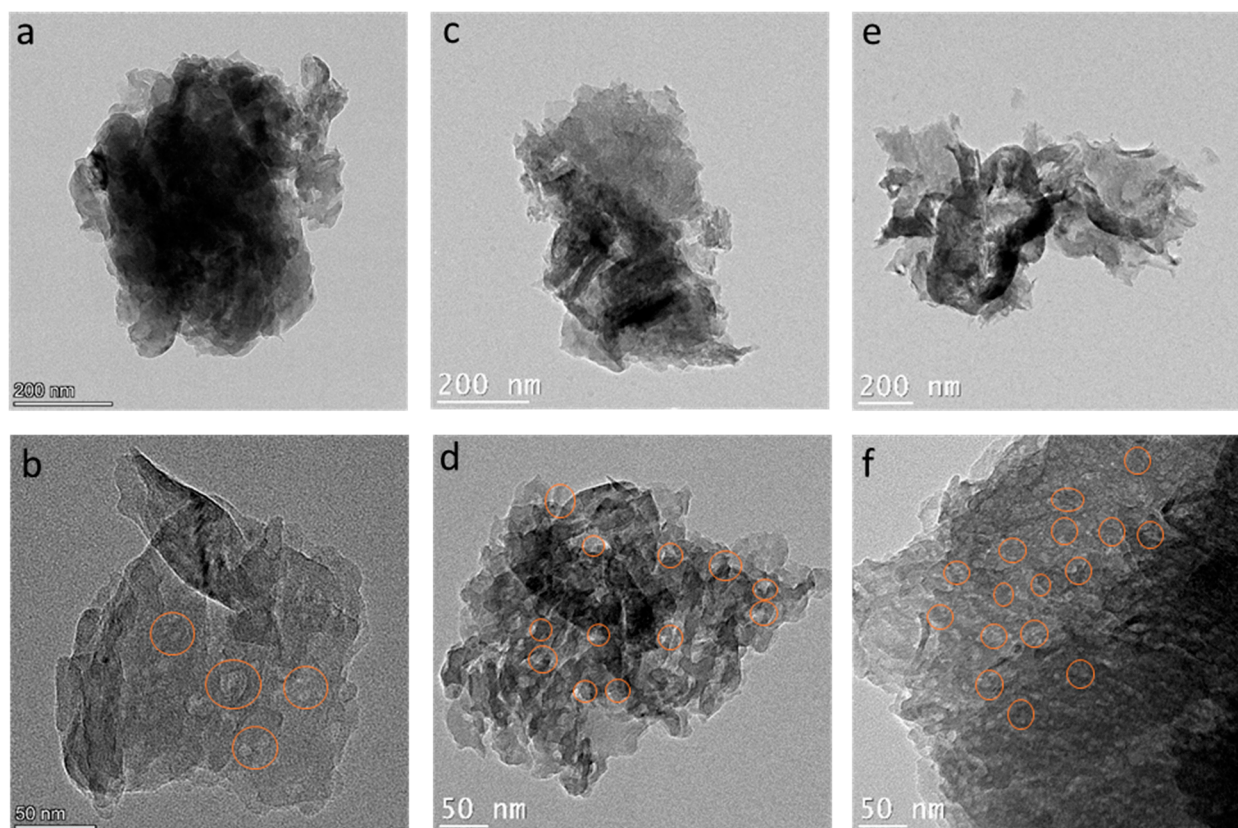


**Figure 1.** TEM images of (a,b) 500-CN, (c,d) 500-UCN, (e,f) 500-AUCN. Orange circles highlight formed pores in these samples.

XRD was employed to investigate the structural characteristics of synthesized samples. As illustrated in Figure 2a, the interlayer stacking of conjugated aromatic C–N heterocycles

is indicated by the strong (002) diffraction peak at  $27.4^\circ$ , present in all the samples. The interplanar tri-s-triazine units are represented by the (100) diffraction peak located at  $13.0^\circ$  [79,80]. After the hydrothermal step performed on BCN, we observed the appearance of an extra peak at  $\sim 10.7^\circ$ . This peak has been attributed to the slight change in alignment of the tri-s-triazine unit arising from the oxidation/hydrolysis of g-C<sub>3</sub>N<sub>4</sub> during the hydrothermal treatment [81,82]. It disappears after the thermal exfoliation, possibly due to the delamination of nanosheets [83]. An enlarged view of the (002) peak is shown in Figure S3. It shows that BCN has a higher intensity of the (002) peak in comparison to other samples. This supports the successful exfoliation of the samples, as evidenced by TEM images (Figure 1). Based on the XRD analysis, we can conclude that the thermal exfoliation and the ultrasonication steps (either in water or acid media) did not significantly affect the interlayer nor interplanar structure of the photocatalysts, as this was also demonstrated elsewhere [84,85].

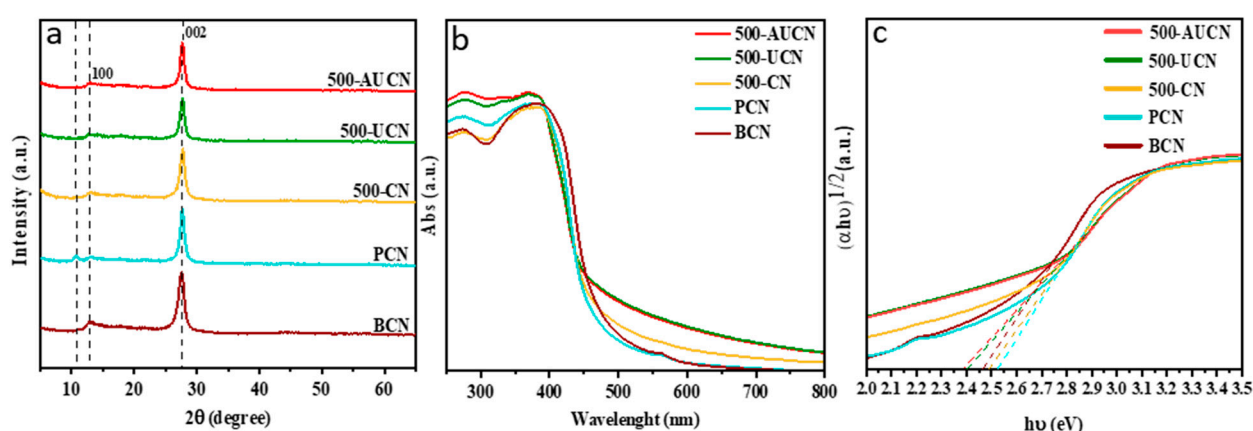


**Figure 2.** (a) XRD patterns, (b) DRS spectra, and (c) Tauc's plot for optical bandgap ( $E_g$ ) analysis of synthesized g-C<sub>3</sub>N<sub>4</sub> samples.

The photocatalytic activity of a material is governed by three main processes: surface redox reactions, the separation and transfer of charges, and light absorption [86–88]. To measure the optical absorption, we conducted UV-vis DRS tests and used the results to estimate the band gap energy of our samples. Figure 2b shows that samples 500-UCN and 500-AUCN (after ultrasonication in water and acid media) present an increased light absorption in both visible and UV regions. This phenomenon could be due to the improved separation and reduced agglomeration of g-C<sub>3</sub>N<sub>4</sub> layers resulting from ultrasonication and acid exfoliation, or because of the defect states' absorption process [89–91]. 550-AUCN shows a further increase in its absorption onset (486 nm), being the sample with the highest and broadest absorption in the visible and UV regions (see Figure S4). The greater utilization of photons could be caused by its improved layered structure after being treated at a higher temperature during the thermal step at  $550^\circ\text{C}$  [92]. In addition, at higher temperatures, the increase in the condensation of N and C atoms leads to the expansion of electron delocalization in the aromatic nanosheets, which is the cause of the enlarged absorption [93]. Figure 2c shows the Tauc's plot (solid lines) derived from the UV-vis DRS measurements and linear extrapolation (dashed lines). The obtained values for the band gaps were 2.39 eV, 2.40 eV, 2.49 eV, 2.52 eV, and 2.46 eV for 500-AUCN, 500-UCN, 500-CN, PCN, and BCN, respectively. It can be observed that both ultrasonication in acid and water resulted in a decrease in the bandgap with respect to 500-CN and PCN, similar to other published work [94]. Previously, it was found that the introduction of structural defects and oxygen-containing functional groups could narrow the band gap of C<sub>3</sub>N<sub>4</sub> [46,95,96]. In particular, N vacancies normally produce mid-gap states in the band gap close to the conduction band, thus narrowing it [97]. We believe it is also the case in our samples, i.e., introduced N vacancies and oxygen-containing functional groups were responsible for

the narrowing of the band gap of 500-AUCN and 500-UCN. On the other hand, 500-CN (2.49 eV) and PCN (2.52 eV) samples showed an increase in band gap energy compared to BCN (2.46 eV), which is due to the quantum confinement effect and could strengthen their redox ability [70,98].

For the photocatalytic reaction to happen, in the first step of the process, pollutants must adsorb onto the surface of the photocatalyst. This is where photogenerated charge carriers initiate redox reactions that will contribute to pollutants' degradation [99,100]. Thus, to enhance the photocatalytic activity, it is important to analyze the surface area and the textural characteristics of the photocatalysts through gas adsorption tests and using the BET theory. The surface area is 61.3 m<sup>2</sup>/g, 62.8 m<sup>2</sup>/g, 53.3 m<sup>2</sup>/g, 53.6 m<sup>2</sup>/g, and 8.82 m<sup>2</sup>/g for 500-AUCN, 500-UCN, 500-CN, PCN, and BCN, respectively. Samples that have undergone ultrasonication in water and acid media (500-UCN and 500-AUCN) present similar surface area (62.8 and 61.3 m<sup>2</sup>/g, respectively), but it is much larger than that of BCN (~7 times). The trend goes as follows: 500-UCN ≈ 500-AUCN > 500-CN ≈ PCN >>> BCN. This suggests that the hydrothermal treatment was able to significantly increase the specific surface area by creating pores, and ultrasonication, whether in water or acid, could further enlarge the specific surface area through mechanical exfoliation. The greater surface area of 500-UCN and 500-AUCN is in line with the enhanced light absorption observed in Figure 2b [98,101]. In addition, 500-AUCN had a smaller average pore size in comparison to the other samples (Figure S5), agreeing with our TEM analysis shown in Figure 1. A general feature was that ultrasonication caused a considerable boost in the number of micro-pores (<2 nm) in 500-UCN and 500-AUCN, while 500-CN had larger pores with fewer micro-pores, in comparison to other porous samples. Based on these characterizations, we proposed that the thermal treatment resulted in thermal etching and an enlarged pore size. In addition, the subsequent sonication step caused the breakdown through larger pores into smaller and thinner nanosheets with more micro-pores and small mesopores (see Figure S5 and Figure 1). But importantly, the sonication time needs to be optimized because excessive ultrasonication, especially in acid media (500-AUCN—40 min), caused a collapse in the structure of g-C<sub>3</sub>N<sub>4</sub> and its pores (Figure S2), and a large performance drop.

XPS was carried out to further explore the changes in the chemical state, elemental composition, and surface functional groups of the as-synthesized samples. Two C1s peaks at 285.2 eV and 288.5 eV were observed (Figure 3a), attributed to the sp<sup>2</sup> C=C bonds of the graphitic C and the adventitious hydrocarbons, and sp<sup>2</sup> C in N-C=N bonds, respectively [102,103]. The deconvolution of N1s peaks (Figure 3b) revealed three distinct components positioned at 401.2 eV, 399.9 eV, and 399.0 eV, corresponding to the N-H<sub>x</sub> group in the heptazine framework, bridging N in -N-(C)<sub>3</sub> (N<sub>3C</sub>), and sp<sup>2</sup> hybridized N in -C-N=C or C-N=C (N<sub>2C</sub>), respectively [104,105]. N<sub>(2C)</sub>/N<sub>(3C)</sub> ratios for 500-AUCN, 500-UCN, and 500-CN were 2.1, 2.8, and 3.3. The reduced ratio of N<sub>(2C)</sub>/N<sub>(3C)</sub> in 500-AUCN suggests the creation of and increase in two-coordinated N vacancies with respect to more stable three-coordinated N atoms [106], perhaps due to the powerful oxidizing properties of nitric acid, further aided through ultrasonication. Figure 3c shows high-resolution spectra for O1s. The two peaks located at 531.9 eV and 533.2 eV are attributed to -C=O/C-O and -OH groups [107,108]. 500-UCN clearly exhibits a higher concentration of -OH groups and 500-CN has a higher concentration of -C=O/C-O, while 500-AUCN shows a similar concentration of -C=O/C-O and -OH groups. Moreover, from the XPS survey spectra, the concentration of oxygen-containing groups in 500-AUCN was the highest among the three samples, being ~1.3 and 2 times that in 500-UCN and 500-CN, respectively, again supporting the fact that the considerable oxidation reaction occurred during the ultrasonication-in-acid process [109]. It suggests that this process led to not only smaller pore sizes but also obvious variations in chemical species.

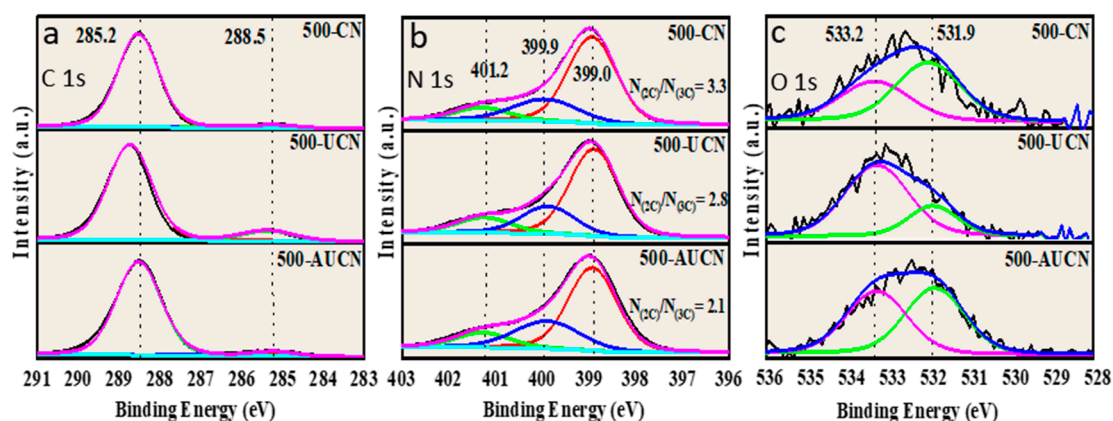


**Figure 3.** (a) C 1s, (b) N 1s, and (c) O 1s XPS spectra of g-C<sub>3</sub>N<sub>4</sub> samples exfoliated at 500 °C.

To assess the photocatalytic activity of the samples, MO degradation was performed under visible light irradiation ( $\lambda > 400$  nm) at room temperature. Figure 4a displays the UV-vis absorption spectra of MO during the photodegradation reaction in the presence of 500-AUCN. The MO absorption peak at  $\sim 464$  nm dramatically decreased to almost zero, indicating its nearly complete degradation after 30 min. Figure 4b shows the MO photodegradation percentage as a function of the reaction time for different samples. 500-AUCN had the greatest activity (red line in Figure 4b), removing 96% of MO in 30 min, and reaching 99% after 1 h, whereas only 50%, 30%, and 13% of MO were removed in 1 h when using 500-UCN, 500-CN, and BCN, respectively. Two control tests were carried out to better assess the photocatalytic performance, (i) MO under visible light irradiation without any photocatalyst and (ii) MO in the presence of the most effective material (500-AUCN), but under dark conditions. No degradation of MO occurred in either of the control tests, suggesting MO removal is not caused by the photocatalyst or light alone, and its degradation is due to the photocatalytic reaction in the presence of our C<sub>3</sub>N<sub>4</sub>-based materials. The  $k$  values (summarized in Table 2) show the trend of 500-AUCN ( $11.2 \times 10^{-3} \text{ mg}^{-1} \text{ min}^{-1}$ ) > 500-UCN ( $2.3 \times 10^{-3} \text{ mg}^{-1} \text{ min}^{-1}$ ) > 500-CN ( $1.4 \times 10^{-3} \text{ mg}^{-1} \text{ min}^{-1}$ ) > BCN ( $0.2 \times 10^{-3} \text{ mg}^{-1} \text{ min}^{-1}$ ). Impressively, the  $k$  value for 500-AUCN is 58 times higher than that of BCN. The MO photodegradation using the photocatalyst samples exfoliated at 550 °C and 600 °C followed the same trend (Figures S6–S8 and Table S1). It is clear that ultrasonication in acid media is beneficial to photocatalysis regardless of the exfoliation temperature (500 °C, 550 °C, and 600 °C). The experiment was conducted four times for the best sample (500-AUCN) over a total duration of 240 min (Figure S9). The photocatalyst exhibited high efficiency in removing MO and demonstrated good stability for photocatalytic applications. Moreover, we would like to remark that the sample 500-AUCN presented the highest photocatalytic performance for MO degradation among all the C<sub>3</sub>N<sub>4</sub>-based materials reported so far (Table S2). We link this to the oxidizing nature of HNO<sub>3</sub>, which, during the sonication process, generated N vacancies and oxygen-containing functional groups in g-C<sub>3</sub>N<sub>4</sub> that can help photocatalysis.

**Table 2.**  $k$  values for the MO photodegradation reaction in the presence of photocatalytic g-C<sub>3</sub>N<sub>4</sub> samples exfoliated at 500 °C.

Sample	$k$ ( $10^{-3} \text{ mg}^{-1} \text{ min}^{-1}$ )
500-AUCN	$11.2 \pm 0.35$
500-UCN	$2.3 \pm 0.48$
500-CN	$1.4 \pm 0.30$

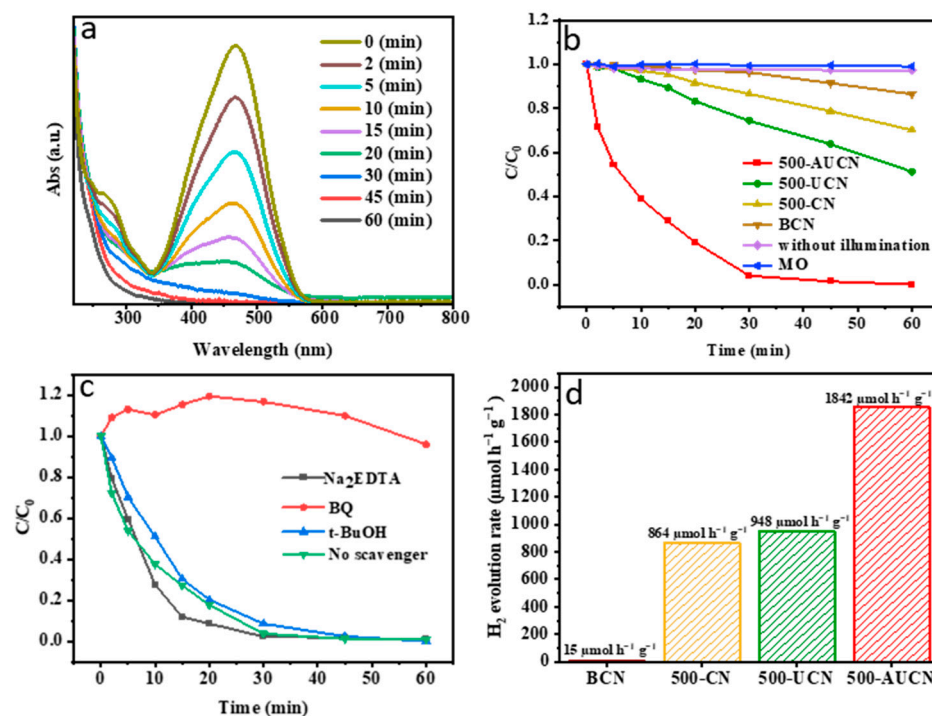


**Figure 4.** (a) UV-vis absorption spectra of MO during the photodegradation process using 500-AUCN, (b) photocatalytic activity test using different  $g\text{-C}_3\text{N}_4$  samples, (c) photocatalytic degradation of MO under visible light, using 500-AUCN in the presence of three different scavengers, and (d) hydrogen evolution rate of samples 500-AUCN, 500-UCN, 500-CN, and BCN under visible light irradiation.

To comprehend the mechanism involved in the degradation of MO, we tested several trapping agents for our benchmark sample, 500-AUCN (Figure 4c). Specifically,  $t\text{-BuOH}$ , BQ, and  $\text{Na}_2\text{EDTA}$  were used to capture  $h^+$ ,  $\bullet\text{O}_2^-$ , and  $\bullet\text{OH}$ , respectively. It was found that the addition of  $\text{Na}_2\text{EDTA}$  and  $t\text{-BuOH}$  had almost no impact on the degradation of MO, which means that  $\bullet\text{OH}$  and  $h^+$  did not play a major role in the photocatalytic process. On the other hand, when BQ was added, the photocatalytic activity was notably reduced, suggesting that  $\bullet\text{O}_2^-$  acted as the primary species responsible for the degradation of MO.

We also tested hydrogen production under visible light for all the as-synthesized samples. As shown in Figure 4d, 500-AUCN once again showed the best performance, with a hydrogen production rate of  $1842 \mu\text{mol h}^{-1} \text{g}^{-1}$ , 120 times higher than that of BCN ( $15 \mu\text{mol h}^{-1} \text{g}^{-1}$ ). Samples 500-UCN and 500-CN also displayed higher photocatalytic activity when compared to BCN, with HER of  $948 \mu\text{mol h}^{-1} \text{g}^{-1}$  and  $864 \mu\text{mol h}^{-1} \text{g}^{-1}$ , respectively.

We also subjected the  $500^\circ\text{C}$  exfoliated samples and BCN to PEC tests and consistently we observed that 500-AUCN and 500-UCN (the ones that underwent sonication in acid and water, respectively) have a greater photocurrent generation compared to 500-CN and BCN (Figure 5a). This suggests that improved samples have a better charge carrier generation and/or transfer to the surface, which could result in a more beneficial photocatalytic activity. Figure 5b displays the results of Electrochemical Impedance Spectroscopy (EIS) measurements on multiple samples. The EIS Nyquist plots of the 500-AUCN and 500-UCN samples show a smaller arc radius when compared to 500-CN and BCN, both in the dark and under irradiation. This indicates that the charge transfer resistance in the former two samples is lower, possibly due to the presence of more functional groups.

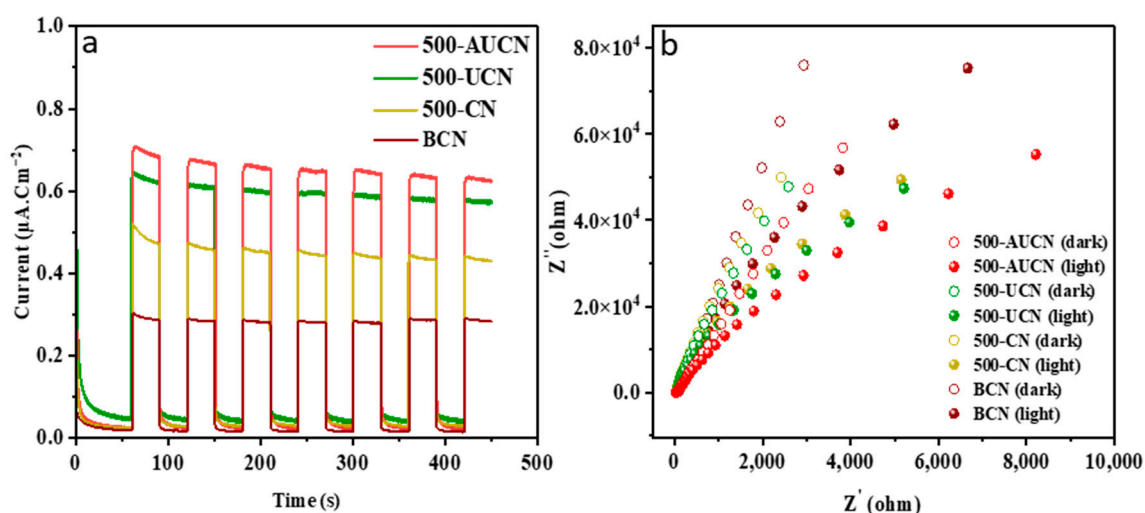


**Figure 5.** (a) Transient photocurrent response of  $g\text{-C}_3\text{N}_4$  samples under a solar simulator and (b) EIS Nyquist plots in the dark and under simulated solar light irradiation of  $g\text{-C}_3\text{N}_4$  samples.

The differences in performance of all samples synthesized in this work are related to their optical, chemical, and surface properties. In this section, we aim to provide a comprehensive analysis of the key properties exhibited by the most efficient sample, while highlighting the modifications that were introduced during the synthetic process. Our goal is also to assist readers in gaining a better understanding of the enhanced photocatalytic behavior, allowing researchers to rationally design and synthesize  $\text{C}_3\text{N}_4$ -based materials. The analysis is performed from the following aspects:

#### I. Optical properties:

Light absorption has a noticeable influence on the semiconductor's performance. 500-AUCN and 500-UCN exhibited a broader light absorption profile within the visible spectrum due to their smaller bandgaps caused by the introduction of defects through ultrasonication in water and acid. Broader light absorption tends to favor the generation of a higher number of electron-hole pairs when subjected to light irradiation, thereby leading to improved photocatalytic properties [110]. This is in agreement with Zhang et al.'s work, where they also found an increased absorption of  $\text{C}_3\text{N}_4$  in the visible region when ultrasonication was performed [70].

#### II. Chemical properties:

The excellent photocatalytic performance of 500-AUCN for MO degradation is highly related to the nature of its surface functional groups ( $-\text{C}=\text{O}/\text{C}-\text{O}$  and  $-\text{OH}$ ) generated through the ultrasonication step in nitric acid. They potentially act as active sites increasing the photocatalytic activity [111]. 500-AUCN showed a higher number of oxygen-containing functional groups based on our XPS studies. According to previous studies [112,113], adding  $-\text{C}=\text{O}/\text{C}-\text{O}$  functional groups can improve the photocatalytic activity of  $g\text{-C}_3\text{N}_4$  by enhancing the hydrophilicity of its surface, the number of active sites, and the effectiveness of charge separation.  $-\text{OH}$  groups could boost the electron transfer in  $\text{C}_3\text{N}_4$  and prevent aggregation of layers by forming interlayer hydrogen bonds, thus improving photocatalytic activity [114]. This could at least serve as one reason for the best performance of 500-AUCN for hydrogen production as well. A hydrogen evolution reaction mostly relies on efficient light absorption and charge separation, followed by effective redox reactions to release hydrogen and oxygen from water [115,116]. Ultrasonication in acid helps these factors by creating defects that narrow the bandgap in the structure of  $g\text{-C}_3\text{N}_4$  [117].

Moreover, the ultrasonication step in acid media, performed in the synthesis of 500-AUCN, resulted in a reduction in the number of  $\text{N}_{2\text{C}}$  atoms relative to  $\text{N}_{3\text{C}}$  atoms when compared to 500-UCN and 500-CN, leading to the creation of N vacancies that enhance its

photocatalytic performance [64,118]. It has been reported that a higher concentration of nitrogen vacancies improves the separation of photogenerated charge carriers and light absorption [119,120]. Furthermore,  $N_{3C}$  has a larger number of unpaired electrons in the nitrogen atoms, resulting in a higher density of active sites available for photocatalytic processes [121]. Wang et al. [104] demonstrated that surface nitrogen vacancies reduce the recombination of photoinduced charge carriers by creating localized electronic trap states within the band gap of the material. This led to an increase in the number of charges that migrated to the photocatalyst surface and participated in following redox reactions to degrade pollutants [117].

### III. Surface properties:

It is well known that ultrasonication helps to separate stacked layers to create 2D materials [122–124]. When ultrasonication was performed on 500-CN ( $53.3 \text{ m}^2/\text{g}$ ), we observed a moderate increase in specific surface area for 500-AUCN and 500-UCN ( $61.4 \text{ m}^2/\text{g}$  and  $62.9 \text{ m}^2/\text{g}$ , respectively). This potentially provided more exposed active sites that are available for the MO adsorption and redox reaction involved in its photodegradation [125].

Furthermore, compared to other samples, 500-AUCN has the smallest pore size. These small and well-distributed pores serve a dual purpose. Firstly, they reduce van der Waals interaction by creating many boundaries. Secondly, they create cross-planar diffusion channels and numerous new active edges. These features accelerate the diffusion and mass transfer of the photogenerated charge carriers to a great extent [126]. The results of a recent study have shown that the size and distribution of pores in porous  $g\text{-C}_3\text{N}_4$  nanosheets play a significant role in the interaction between the semiconductor and organic pollutants during the photocatalytic process [127]. Specifically, microporous and small mesoporous structures, which were also observed in 500-AUCN, are beneficial for the mass transfer and molecular diffusion of reactants to the active sites of the  $\text{C}_3\text{N}_4$  semiconductor [128]. Due to the reduction in pore size and number of stacked nanosheet layers, the number of active sites for photocatalytic reactions increases and bulk diffusion length to the active sites decreases, thereby lowering the probability of recombination among photoexcited charge carriers [129,130].

## 4. Conclusions

We developed an optimized procedure to synthesize porous ultra-thin  $g\text{-C}_3\text{N}_4$  nanosheets that involved the combination of a thermal step at  $500^\circ\text{C}$  and ultrasonication in acid. This method was the most effective in exfoliating  $\text{C}_3\text{N}_4$ , yielding ultra-thin nanosheets with high photocatalytic performance. It reduced the time and energy required for exfoliation while producing ultra-thin nanosheets with small, well-distributed pores. We achieved an impressive  $k$  value of  $11.2 \times 10^{-3} \text{ mg}^{-1} \text{ min}^{-1}$  for the photodegradation of MO when using 500-AUCN. This is the highest value known to date utilizing  $\text{C}_3\text{N}_4$ -based materials for MO degradation. This was due to the combination effect of its porous thin layered structure, increased light absorption, nitrogen vacancies, and oxygen-containing functional groups created through ultrasonication in acid. Hydrogen production was also performed for the as-synthesized samples. The best production rate was also achieved for 500-AUCN ( $1842 \mu\text{mol h}^{-1} \text{ g}^{-1}$ ). This indicates that this sample is suitable for both applications. This study presents an efficient method for exfoliating  $\text{C}_3\text{N}_4$ -based materials, with high photocatalytic performance that paves the way to tackle the organic matter pollution and provides an alternative to non-renewable energy sources.

**Supplementary Materials:** The following supporting information can be downloaded at: <https://www.mdpi.com/article/10.3390/nano14010103/s1>, Figure S1: TEM images of thermally exfoliated  $g\text{-C}_3\text{N}_4$  samples: (a and b) 550-CN and (c and d) 600-CN; Figure S2:  $g\text{-C}_3\text{N}_4$  sample ultrasonicated in acid media for 40 min; Figure S3: Enlarged view of (002) peak of XRD for  $g\text{-C}_3\text{N}_4$  samples; Figure S4: DRS spectra of  $g\text{-C}_3\text{N}_4$  samples prepared under different conditions; Figure S5: Pore size distribution curves of different  $g\text{-C}_3\text{N}_4$  samples; Figure S6: Visible light degradation spectra of MO using samples (a) 500-CN, (b) 500-UCN, (c) 550-CN, (d) 550-UCN, (e) 550-AUCN, (f) 600-CN, (g) 600-UCN, and

(h) 600-AUCN; Figure S7: Photocatalytic degradation of MO under visible light using photocatalyst samples exfoliated at 550 °C; Figure S8: Photocatalytic degradation of MO under visible light, using photocatalyst samples exfoliated at 600 °C; Figure S9: Photocatalytic stability of 500-AUCN in four successive cycling reactions under visible light irradiation; Table S1: Normalized reaction rate ( $k$ ) values for the MO photodegradation reaction in the presence of photocatalytic samples exfoliated at 550 °C and 600 °C; Table S2: Performance of C<sub>3</sub>N<sub>4</sub>-based samples for degradation of MO under visible light irradiation in recently published literature. References [131–141] are cited in the Supplementary Materials.

**Author Contributions:** Z.K.B. performed methodology, experiments, data collection, data analysis, and manuscript writing. C.R.-S. performed data analysis, manuscript review, editing, and supervision. A.Y. carried out manuscript review and supervision. D.M. performed conceptualization, funding acquisition, resource management, manuscript review, editing, and supervision. All authors have read and agreed to the published version of the manuscript.

**Funding:** This work is supported by the Natural Sciences and Engineering Research Council of Canada (NSERC, RGPIN-2020-05921) and le Fonds de Recherche du Québec-Nature et Technologies (FRQNT, 2018-RS-203321). D.M. is grateful to the Canada Research Chairs Program (CRC-2019-00253). C.R.-S. thanks Fonds de recherche du Québec-Nature et technologies (FRQNT) B3X program for its financial support.

**Data Availability Statement:** Data are contained within the article and Supplementary Materials.

**Conflicts of Interest:** The authors declare no conflicts of interest.

## References

1. Shi, Y.; Zhao, Q.; Li, J.; Gao, G.; Zhi, J. Onion-Liked Carbon-Embedded Graphitic Carbon Nitride for Enhanced Photocatalytic Hydrogen Evolution and Dye Degradation. *Appl. Catal. B Environ.* **2022**, *308*, 121216. [[CrossRef](#)]
2. Li, X.; Wu, J.; An, S.; Li, K.; Zhang, J.; Pei, M.; Song, C.; Guo, X. Ultrathin Crystalline Carbon Nitride Nanosheets for Highly Efficient Photocatalytic Pollutant Removal and Hydrogen Production. *ACS Appl. Nano Mater.* **2023**, *6*, 11601–11611. [[CrossRef](#)]
3. Gaikwad, R.P.; Naikwadi, D.R.; Biradar, A.V.; Gawande, M.B. Photocatalytic One-Pot Conversion of Aldehydes to Esters and Degradation of Rhodamine B Dye Using Mesoporous Graphitic Carbon Nitride. *ACS Appl. Nano Mater.* **2023**, *6*, 1859–1869. [[CrossRef](#)]
4. Zhao, C.; Sun, H.; Li, C.; Wang, M.; Wu, J.; Chen, M.; Jiang, S.; Niu, T.; Liu, D. Facile Synthesis of 3D Interconnected Porous G-C<sub>3</sub>N<sub>4</sub>/rGO Composite for Hydrogen Production and Dye Elimination. *Catalysts* **2023**, *13*, 1079. [[CrossRef](#)]
5. Chen, H.; Wang, Y.; Ye, J.; Cao, Z.; Zhu, K.; Yang, H.; Xu, Z. Oxygen-Doped Protonated C<sub>3</sub>N<sub>4</sub> Nanosheet as Particle Electrode and Photocatalyst to Degrade Dye by Photoelectrocatalytic Oxidation Process. *Sep. Purif. Technol.* **2023**, *312*, 123405. [[CrossRef](#)]
6. Huang, L.; Xu, H.; Li, Y.; Li, H.; Cheng, X.; Xia, J.; Xu, Y.; Cai, G. Visible-Light-Induced WO<sub>3</sub>/g-C<sub>3</sub>N<sub>4</sub> Composites with Enhanced Photocatalytic Activity. *Dalton Trans.* **2013**, *42*, 8606. [[CrossRef](#)] [[PubMed](#)]
7. Liang, L.; Shi, L.; Wang, F.; Yao, L.; Zhang, Y.; Qi, W. Synthesis and Photo-Catalytic Activity of Porous g-C<sub>3</sub>N<sub>4</sub>: Promotion Effect of Nitrogen Vacancy in H<sub>2</sub> Evolution and Pollutant Degradation Reactions. *Int. J. Hydrogen Energy* **2019**, *44*, 16315–16326. [[CrossRef](#)]
8. Zhu, W.; Yue, Y.; Wang, H.; Zhang, B.; Hou, R.; Xiao, J.; Huang, X.; Ishag, A.; Sun, Y. Recent Advances on Energy and Environmental Application of Graphitic Carbon Nitride (g-C<sub>3</sub>N<sub>4</sub>)-Based Photocatalysts: A Review. *J. Environ. Chem. Eng.* **2023**, *11*, 110164. [[CrossRef](#)]
9. Dawood, F.; Anda, M.; Shafiullah, G.M. Hydrogen Production for Energy: An Overview. *Int. J. Hydrogen Energy* **2020**, *45*, 3847–3869. [[CrossRef](#)]
10. Mirhosseininia, J.; Sabbaghi, S.; Mirbagheri, N.S.; Zerafat, M.M. Treatment of As-Contaminated Drinking Water Using a Nano Zero-Valent Iron/Copper Slag Nanocomposite. *J. Water Process Eng.* **2022**, *49*, 103011. [[CrossRef](#)]
11. Khanzada, N.K.; Farid, M.U.; Kharraz, J.A.; Choi, J.; Tang, C.Y.; Nghiem, L.D.; Jang, A.; An, A.K. Removal of Organic Micropollutants Using Advanced Membrane-Based Water and Wastewater Treatment: A Review. *J. Membr. Sci.* **2020**, *598*, 117672. [[CrossRef](#)]
12. Sirés, I.; Brillas, E. Remediation of Water Pollution Caused by Pharmaceutical Residues Based on Electrochemical Separation and Degradation Technologies: A Review. *Environ. Int.* **2012**, *40*, 212–229. [[CrossRef](#)] [[PubMed](#)]
13. Rasouli, K.; Rasouli, J.; Mohtaram, M.S.; Sabbaghi, S.; Kamyab, H.; Moradi, H.; Chelliapan, S. Biomass-Derived Activated Carbon Nanocomposites for Cleaner Production: A Review on Aspects of Photocatalytic Pollutant Degradation. *J. Clean. Prod.* **2023**, *419*, 138181. [[CrossRef](#)]
14. Bai, Y.; Hippalgaonkar, K.; Sprick, R.S. Organic Materials as Photocatalysts for Water Splitting. *J. Mater. Chem. A* **2021**, *9*, 16222–16232. [[CrossRef](#)]
15. Chen, L.; Maigbay, M.A.; Li, M.; Qiu, X. Synthesis and Modification Strategies of G-C<sub>3</sub>N<sub>4</sub> Nanosheets for Photocatalytic Applications. *Adv. Powder Mater.* **2024**, *3*, 100150. [[CrossRef](#)]

16. Jiao, X.; Zheng, K.; Hu, Z.; Sun, Y.; Xie, Y. Broad-Spectral-Response Photocatalysts for CO<sub>2</sub> Reduction. *ACS Cent. Sci.* **2020**, *6*, 653–660. [[CrossRef](#)] [[PubMed](#)]
17. Bhowmik, S.; Phukan, S.J.; Sah, N.K.; Roy, M.; Garai, S.; Iyer, P.K. Review of Graphitic Carbon Nitride and Its Composite Catalysts for Selective Reduction of CO<sub>2</sub>. *ACS Appl. Nano Mater.* **2021**, *4*, 12845–12890. [[CrossRef](#)]
18. Sun, B.; Lu, S.; Qian, Y.; Zhang, X.; Tian, J. Recent Progress in Research and Design Concepts for the Characterization, Testing, and Photocatalysts for Nitrogen Reduction Reaction. *Carbon Energy* **2023**, *5*, e305. [[CrossRef](#)]
19. Zhang, Q.; Li, Q.; Li, H.; Shi, X.; Zhou, Y.; Ye, Q.; Yang, R.; Li, D.; Jiang, D. Synergistic Effects of the Ni<sub>3</sub>B Cocatalyst and N Vacancy on g-C<sub>3</sub>N<sub>4</sub> for Effectively Enhanced Photocatalytic N<sub>2</sub> Fixation. *Inorg. Chem.* **2023**, *62*, 12138–12147. [[CrossRef](#)]
20. Yang, X.; Wang, D. Photocatalysis: From Fundamental Principles to Materials and Applications. *ACS Appl. Energy Mater.* **2018**, *1*, 6657–6693. [[CrossRef](#)]
21. Li, P.; Wang, J.; Wang, Y.; Dong, L.; Wang, W.; Geng, R.; Ding, Z.; Luo, D.; Pan, D.; Liang, J.; et al. Ultrafast Recovery of Aqueous Uranium: Photocatalytic U(VI) Reduction over CdS/g-C<sub>3</sub>N<sub>4</sub>. *Chem. Eng. J.* **2021**, *425*, 131552. [[CrossRef](#)]
22. Xu, C.; Ravi Anusuyadevi, P.; Aymonier, C.; Luque, R.; Marre, S. Nanostructured Materials for Photocatalysis. *Chem. Soc. Rev.* **2019**, *48*, 3868–3902. [[CrossRef](#)] [[PubMed](#)]
23. Akpan, U.G.; Hameed, B.H. Parameters Affecting the Photocatalytic Degradation of Dyes Using TiO<sub>2</sub>-Based Photocatalysts: A Review. *J. Hazard. Mater.* **2009**, *170*, 520–529. [[CrossRef](#)] [[PubMed](#)]
24. Akerdi, A.G.; Bahrami, S.H. Application of Heterogeneous Nano-Semiconductors for Photocatalytic Advanced Oxidation of Organic Compounds: A Review. *J. Environ. Chem. Eng.* **2019**, *7*, 103283. [[CrossRef](#)]
25. Chen, D.; Cheng, Y.; Zhou, N.; Chen, P.; Wang, Y.; Li, K.; Huo, S.; Cheng, P.; Peng, P.; Zhang, R.; et al. Photocatalytic Degradation of Organic Pollutants Using TiO<sub>2</sub>-Based Photocatalysts: A Review. *J. Clean. Prod.* **2020**, *268*, 121725. [[CrossRef](#)]
26. Gadore, V.; Mishra, S.R.; Ahmaruzzaman, M. Metal Sulphides and Their Heterojunctions for Photocatalytic Degradation of Organic Dyes-A Comprehensive Review. *Environ. Sci. Pollut. Res.* **2023**, *30*, 90410–90457. [[CrossRef](#)] [[PubMed](#)]
27. Sun, Y.; Zhang, W.; Li, Q.; Liu, H.; Wang, X. Preparations and Applications of Zinc Oxide Based Photocatalytic Materials. *Adv. Sens. Energy Mater.* **2023**, *2*, 100069. [[CrossRef](#)]
28. Cheng, L.; Xiang, Q.; Liao, Y.; Zhang, H. CdS-Based Photocatalysts. *Energy Environ. Sci.* **2018**, *11*, 1362–1391. [[CrossRef](#)]
29. Okoye, P.C.; Azi, S.O.; Qahtan, T.F.; Owolabi, T.O.; Saleh, T.A. Synthesis, Properties, and Applications of Doped and Undoped CuO and Cu<sub>2</sub>O Nanomaterials. *Mater. Today Chem.* **2023**, *30*, 101513. [[CrossRef](#)]
30. Zhang, J.-H.; Wei, M.-J.; Wei, Z.-W.; Pan, M.; Su, C.-Y. Ultrathin Graphitic Carbon Nitride Nanosheets for Photocatalytic Hydrogen Evolution. *ACS Appl. Nano Mater.* **2020**, *3*, 1010–1018. [[CrossRef](#)]
31. Wu, Y.; Wang, H.; Tu, W.; Liu, Y.; Tan, Y.Z.; Yuan, X.; Chew, J.W. Quasi-Polymeric Construction of Stable Perovskite-Type LaFeO<sub>3</sub>/g-C<sub>3</sub>N<sub>4</sub> Heterostructured Photocatalyst for Improved Z-Scheme Photocatalytic Activity via Solid p-n Heterojunction Interfacial Effect. *J. Hazard. Mater.* **2018**, *347*, 412–422. [[CrossRef](#)] [[PubMed](#)]
32. Zhang, Q.; Liu, X.; Chaker, M.; Ma, D. Advancing Graphitic Carbon Nitride-Based Photocatalysts toward Broadband Solar Energy Harvesting. *ACS Mater. Lett.* **2021**, *3*, 663–697. [[CrossRef](#)]
33. Xu, J.; Gao, Q.; Wang, Z. Porous G-C<sub>3</sub>N<sub>4</sub> Nanosheets for On–Off–On Fluorescence Detection and Elimination of Chromium(VI) and Sulfite. *ACS Appl. Nano Mater.* **2023**, *6*, 750–758. [[CrossRef](#)]
34. Zhu, Q.; Xu, Z.; Qiu, B.; Xing, M.; Zhang, J. Emerging Cocatalysts on g-C<sub>3</sub>N<sub>4</sub> for Photocatalytic Hydrogen Evolution. *Small* **2021**, *17*, 2101070. [[CrossRef](#)] [[PubMed](#)]
35. Chen, Y.; Cheng, M.; Lai, C.; Wei, Z.; Zhang, G.; Li, L.; Tang, C.; Du, L.; Wang, G.; Liu, H. The Collision between g-C<sub>3</sub>N<sub>4</sub> and QDs in the Fields of Energy and Environment: Synergistic Effects for Efficient Photocatalysis. *Small* **2023**, *19*, 2205902. [[CrossRef](#)] [[PubMed](#)]
36. Hayat, A.; Sohail, M.; El Jery, A.; Al-Zaydi, K.M.; Alshammari, K.F.; Khan, J.; Ali, H.; Ajmal, Z.; Taha, T.A.; Ud Din, I.; et al. Different Dimensionalities, Morphological Advancements and Engineering of g-C<sub>3</sub>N<sub>4</sub>-Based Nanomaterials for Energy Conversion and Storage. *Chem. Rec.* **2023**, *23*, e202200171. [[CrossRef](#)] [[PubMed](#)]
37. Zhuang, H.; Lin, L.; Xu, M.; Xu, W.; Liu, X. Construction of G-C<sub>3</sub>N<sub>4</sub>-Based Photoelectrodes towards Photoelectrochemical Water Splitting: A Review. *J. Alloys Compd.* **2023**, *969*, 172302. [[CrossRef](#)]
38. Zhang, X.; Yang, P. g-C<sub>3</sub>N<sub>4</sub> Nanosheet Nanoarchitectonics: H<sub>2</sub> Generation and CO<sub>2</sub> Reduction. *ChemNanoMat* **2023**, *9*, e202300041. [[CrossRef](#)]
39. Li, Y.; Ouyang, S.; Xu, H.; Hou, W.; Zhao, M.; Chen, H.; Ye, J. Targeted Exfoliation and Reassembly of Polymeric Carbon Nitride for Efficient Photocatalysis. *Adv. Funct. Mater.* **2019**, *29*, 1901024. [[CrossRef](#)]
40. Walter, M.G.; Warren, E.L.; McKone, J.R.; Boettcher, S.W.; Mi, Q.; Santori, E.A.; Lewis, N.S. Solar Water Splitting Cells. *Chem. Rev.* **2010**, *110*, 6446–6473. [[CrossRef](#)]
41. Liao, G.; Li, C.; Li, X.; Fang, B. Emerging Polymeric Carbon Nitride Z-Scheme Systems for Photocatalysis. *Cell Rep. Phys. Sci.* **2021**, *2*, 100355. [[CrossRef](#)]
42. Guo, R.; Wang, J.; Bi, Z.; Chen, X.; Hu, X.; Pan, W. Recent Advances and Perspectives of g-C<sub>3</sub>N<sub>4</sub>-Based Materials for Photocatalytic Dyes Degradation. *Chemosphere* **2022**, *295*, 133834. [[CrossRef](#)] [[PubMed](#)]
43. Tipplook, M.; Panomsuwan, G.; Sudare, T.; Teshima, K. Graphitic Carbon Nitride Nanoflakes Decorated on Multielement-Doped Carbon as Photocatalysts for Bacterial Disinfection under Visible and Near-Infrared Light. *ACS Appl. Nano Mater.* **2022**, *5*, 3422–3433. [[CrossRef](#)]

44. Huo, X.; Yi, H.; Fu, Y.; An, Z.; Qin, L.; Liu, X.; Li, B.; Liu, S.; Li, L.; Zhang, M.; et al. Porous Graphitic Carbon Nitride Nanomaterials for Water Treatment. *Environ. Sci. Nano* **2021**, *8*, 1835–1862. [[CrossRef](#)]
45. Hasija, V.; Raizada, P.; Sudhaik, A.; Sharma, K.; Kumar, A.; Singh, P.; Jonnalagadda, S.B.; Thakur, V.K. Recent Advances in Noble Metal Free Doped Graphitic Carbon Nitride Based Nanohybrids for Photocatalysis of Organic Contaminants in Water: A Review. *Appl. Mater. Today* **2019**, *15*, 494–524. [[CrossRef](#)]
46. Bai, S.; Zhang, N.; Gao, C.; Xiong, Y. Defect Engineering in Photocatalytic Materials. *Nano Energy* **2018**, *53*, 296–336. [[CrossRef](#)]
47. Wang, Y.; Zhong, S.; Niu, Z.; Dai, Y.; Li, J. Synthesis and Up-to-Date Applications of 2D Microporous g-C<sub>3</sub>N<sub>4</sub> Nanomaterials for Sustainable Development. *Chem. Commun.* **2023**, *59*, 10883–10911. [[CrossRef](#)] [[PubMed](#)]
48. Cheng, C.-Q.; Feng, Y.; Shi, Z.-Z.; Zhou, Y.-L.; Kang, W.-J.; Li, Z.; Mao, J.; Shen, G.-R.; Dong, C.-K.; Liu, H.; et al. Highly Conjugated Graphitic Carbon Nitride Nanofoam for Photocatalytic Hydrogen Evolution. *Langmuir* **2022**, *38*, 1471–1478. [[CrossRef](#)]
49. Prasad, C.; Madkhali, N.; Govinda, V.; Choi, H.Y.; Bahadur, I.; Sangaraju, S. Recent Progress on the Development of G-C<sub>3</sub>N<sub>4</sub> Based Composite Material and Their Photocatalytic Application of CO<sub>2</sub> Reductions. *J. Environ. Chem. Eng.* **2023**, *11*, 109727. [[CrossRef](#)]
50. Wang, S.; Li, Y.; Wang, X.; Zi, G.; Zhou, C.; Liu, B.; Liu, G.; Wang, L.; Huang, W. One-Step Supramolecular Preorganization Constructed Crinkly Graphitic Carbon Nitride Nanosheets with Enhanced Photocatalytic Activity. *J. Mater. Sci. Technol.* **2022**, *104*, 155–162. [[CrossRef](#)]
51. Xing, Y.; Wang, X.; Hao, S.; Zhang, X.; Wang, X.; Ma, W.; Zhao, G.; Xu, X. Recent Advances in the Improvement of G-C<sub>3</sub>N<sub>4</sub> Based Photocatalytic Materials. *Chin. Chem. Lett.* **2021**, *32*, 13–20. [[CrossRef](#)]
52. He, B.; Feng, M.; Chen, X.; Sun, J. Multidimensional (0D-3D) Functional Nanocarbon: Promising Material to Strengthen the Photocatalytic Activity of Graphitic Carbon Nitride. *Green Energy Environ.* **2021**, *6*, 823–845. [[CrossRef](#)]
53. Luo, B.; Liu, G.; Wang, L. Recent Advances in 2D Materials for Photocatalysis. *Nanoscale* **2016**, *8*, 6904–6920. [[CrossRef](#)] [[PubMed](#)]
54. Stefa, S.; Griniezi, M.; Dimitropoulos, M.; Paterakis, G.; Galiotis, C.; Kiriakidis, G.; Klontzas, E.; Konsolakis, M.; Binas, V. Highly Porous Thin-Layer g-C<sub>3</sub>N<sub>4</sub> Nanosheets with Enhanced Adsorption Capacity. *ACS Appl. Nano Mater.* **2023**, *6*, 1732–1743. [[CrossRef](#)]
55. Zhang, H.; Liu, J.; Jiang, L. Photocatalytic Hydrogen Evolution Based on Carbon Nitride and Organic Semiconductors. *Nanotechnology* **2022**, *33*, 322001. [[CrossRef](#)] [[PubMed](#)]
56. Mehtab, A.; Alshehri, S.M.; Ahmad, T. Photocatalytic and Photoelectrocatalytic Water Splitting by Porous G-C<sub>3</sub>N<sub>4</sub> Nanosheets for Hydrogen Generation. *ACS Appl. Nano Mater.* **2022**, *5*, 12656–12665. [[CrossRef](#)]
57. Zhang, Y.; Huang, Z.; Dong, C.-L.; Shi, J.; Cheng, C.; Guan, X.; Zong, S.; Luo, B.; Cheng, Z.; Wei, D.; et al. Synergistic Effect of Nitrogen Vacancy on Ultrathin Graphitic Carbon Nitride Porous Nanosheets for Highly Efficient Photocatalytic H<sub>2</sub> Evolution. *Chem. Eng. J.* **2022**, *431*, 134101. [[CrossRef](#)]
58. Zhao, X.; Liu, Q.; Li, X.; Ji, H.; Shen, Z. Two-Dimensional g-C<sub>3</sub>N<sub>4</sub> Nanosheets-Based Photo-Catalysts for Typical Sustainable Processes. *Chin. Chem. Lett.* **2023**, *34*, 108306. [[CrossRef](#)]
59. Zhang, M.; Yang, Y.; An, X.; Hou, L. A Critical Review of G-C<sub>3</sub>N<sub>4</sub>-Based Photocatalytic Membrane for Water Purification. *Chem. Eng. J.* **2021**, *412*, 128663. [[CrossRef](#)]
60. Shi, L.; Chang, K.; Zhang, H.; Hai, X.; Yang, L.; Wang, T.; Ye, J. Drastic Enhancement of Photocatalytic Activities over Phosphoric Acid Protonated Porous g-C<sub>3</sub>N<sub>4</sub> Nanosheets under Visible Light. *Small* **2016**, *12*, 4431–4439. [[CrossRef](#)]
61. Papailias, I.; Todorova, N.; Giannakopoulou, T.; Ioannidis, N.; Boukos, N.; Athanasekou, C.P.; Dimotikali, D.; Trapalis, C. Chemical vs Thermal Exfoliation of G-C<sub>3</sub>N<sub>4</sub> for NO<sub>x</sub> Removal under Visible Light Irradiation. *Appl. Catal. B Environ.* **2018**, *239*, 16–26. [[CrossRef](#)]
62. Xu, J.; Zhang, L.; Shi, R.; Zhu, Y. Chemical Exfoliation of Graphitic Carbon Nitride for Efficient Heterogeneous Photocatalysis. *J. Mater. Chem. A* **2013**, *1*, 14766. [[CrossRef](#)]
63. Nguyen, T.K.A.; Pham, T.-T.; Nguyen-Phu, H.; Shin, E.W. The Effect of Graphitic Carbon Nitride Precursors on the Photocatalytic Dye Degradation of Water-Dispersible Graphitic Carbon Nitride Photocatalysts. *Appl. Surf. Sci.* **2021**, *537*, 148027. [[CrossRef](#)]
64. Huang, J.; Cao, Y.; Wang, H.; Yu, H.; Peng, F.; Zou, H.; Liu, Z. Revealing Active-Site Structure of Porous Nitrogen-Defected Carbon Nitride for Highly Effective Photocatalytic Hydrogen Evolution. *Chem. Eng. J.* **2019**, *373*, 687–699. [[CrossRef](#)]
65. Zhang, D.; Guo, Y.; Zhao, Z. Porous Defect-Modified Graphitic Carbon Nitride via a Facile One-Step Approach with Significantly Enhanced Photocatalytic Hydrogen Evolution under Visible Light Irradiation. *Appl. Catal. B Environ.* **2018**, *226*, 1–9. [[CrossRef](#)]
66. Niu, P.; Liu, G.; Cheng, H.-M. Nitrogen Vacancy-Promoted Photocatalytic Activity of Graphitic Carbon Nitride. *J. Phys. Chem. C* **2012**, *116*, 11013–11018. [[CrossRef](#)]
67. Huang, H.; Jiang, L.; Yang, J.; Zhou, S.; Yuan, X.; Liang, J.; Wang, H.; Wang, H.; Bu, Y.; Li, H. Synthesis and Modification of Ultrathin G-C<sub>3</sub>N<sub>4</sub> for Photocatalytic Energy and Environmental Applications. *Renew. Sustain. Energy Rev.* **2023**, *173*, 113110. [[CrossRef](#)]
68. Moradi, S.; Rodriguez-Seco, C.; Hayati, F.; Ma, D. Sonophotocatalysis with Photoactive Nanomaterials for Wastewater Treatment and Bacteria Disinfection. *ACS Nanosci. Au* **2023**, *3*, 103–129. [[CrossRef](#)]
69. Wang, J.; Wang, S. A Critical Review on Graphitic Carbon Nitride (g-C<sub>3</sub>N<sub>4</sub>)-Based Materials: Preparation, Modification and Environmental Application. *Coord. Chem. Rev.* **2022**, *453*, 214338. [[CrossRef](#)]
70. Zhang, X.; Xie, X.; Wang, H.; Zhang, J.; Pan, B.; Xie, Y. Enhanced Photoresponsive Ultrathin Graphitic-Phase C<sub>3</sub>N<sub>4</sub> Nanosheets for Bioimaging. *J. Am. Chem. Soc.* **2013**, *135*, 18–21. [[CrossRef](#)]

71. Huang, H.; Xiao, K.; Tian, N.; Dong, F.; Zhang, T.; Du, X.; Zhang, Y. Template-Free Precursor-Surface-Etching Route to Porous, Thin g-C<sub>3</sub>N<sub>4</sub> Nanosheets for Enhancing Photocatalytic Reduction and Oxidation Activity. *J. Mater. Chem. A* **2017**, *5*, 17452–17463. [[CrossRef](#)]
72. Li, Y.; Li, X.; Zhang, H.; Xiang, Q. Porous Graphitic Carbon Nitride for Solar Photocatalytic Applications. *Nanoscale Horiz.* **2020**, *5*, 765–786. [[CrossRef](#)] [[PubMed](#)]
73. Dong, J.; Zhang, Y.; Hussain, M.I.; Zhou, W.; Chen, Y.; Wang, L.-N. G-C<sub>3</sub>N<sub>4</sub>: Properties, Pore Modifications, and Photocatalytic Applications. *Nanomaterials* **2021**, *12*, 121. [[CrossRef](#)] [[PubMed](#)]
74. Zhang, X.-S.; Hu, J.-Y.; Jiang, H. Facile Modification of a Graphitic Carbon Nitride Catalyst to Improve Its Photoreactivity under Visible Light Irradiation. *Chem. Eng. J.* **2014**, *256*, 230–237. [[CrossRef](#)]
75. Leong, K.H.; Lim, P.F.; Sim, L.C.; Punia, V.; Pichiah, S. Improved Solar Light Stimulated Charge Separation of G-C<sub>3</sub>N<sub>4</sub> through Self-Altering Acidic Treatment. *Appl. Surf. Sci.* **2018**, *430*, 355–361. [[CrossRef](#)]
76. Lin, L.-S.; Cong, Z.-X.; Li, J.; Ke, K.-M.; Guo, S.-S.; Yang, H.-H.; Chen, G.-N. Graphitic-Phase C<sub>3</sub>N<sub>4</sub> Nanosheets as Efficient Photosensitizers and pH-Responsive Drug Nanocarriers for Cancer Imaging and Therapy. *J. Mater. Chem. B* **2014**, *2*, 1031. [[CrossRef](#)] [[PubMed](#)]
77. Wu, M.; Yan, J.-M.; Zhang, X.; Zhao, M. Synthesis of G-C<sub>3</sub>N<sub>4</sub> with Heating Acetic Acid Treated Melamine and Its Photocatalytic Activity for Hydrogen Evolution. *Appl. Surf. Sci.* **2015**, *354*, 196–200. [[CrossRef](#)]
78. Miao, H.; Zhang, G.; Hu, X.; Mu, J.; Han, T.; Fan, J.; Zhu, C.; Song, L.; Bai, J.; Hou, X. A Novel Strategy to Prepare 2D G-C<sub>3</sub>N<sub>4</sub> Nanosheets and Their Photoelectrochemical Properties. *J. Alloys Compd.* **2017**, *690*, 669–676. [[CrossRef](#)]
79. Bojdys, M.J.; Müller, J.; Antonietti, M.; Thomas, A. Ionothermal Synthesis of Crystalline, Condensed, Graphitic Carbon Nitride. *Chem. A Eur. J* **2008**, *14*, 8177–8182. [[CrossRef](#)]
80. Hong, Z.; Shen, B.; Chen, Y.; Lin, B.; Gao, B. Enhancement of Photocatalytic H<sub>2</sub> Evolution over Nitrogen-Deficient Graphitic Carbon Nitride. *J. Mater. Chem. A* **2013**, *1*, 11754. [[CrossRef](#)]
81. Ming, L.; Yue, H.; Xu, L.; Chen, F. Hydrothermal Synthesis of Oxidized G-C<sub>3</sub>N<sub>4</sub> and Its Regulation of Photocatalytic Activity. *J. Mater. Chem. A* **2014**, *2*, 19145–19149. [[CrossRef](#)]
82. Bai, X.; Wang, L.; Zong, R.; Zhu, Y. Photocatalytic Activity Enhanced via G-C<sub>3</sub>N<sub>4</sub> Nanoplates to Nanorods. *J. Phys. Chem. C* **2013**, *117*, 9952–9961. [[CrossRef](#)]
83. Xu, J.; Wang, Z.; Zhu, Y. Enhanced Visible-Light-Driven Photocatalytic Disinfection Performance and Organic Pollutant Degradation Activity of Porous g-C<sub>3</sub>N<sub>4</sub> Nanosheets. *ACS Appl. Mater. Interfaces* **2017**, *9*, 27727–27735. [[CrossRef](#)] [[PubMed](#)]
84. Ma, T.Y.; Tang, Y.; Dai, S.; Qiao, S.Z. Proton-Functionalized Two-Dimensional Graphitic Carbon Nitride Nanosheet: An Excellent Metal-/Label-Free Biosensing Platform. *Small* **2014**, *10*, 2382–2389. [[CrossRef](#)] [[PubMed](#)]
85. Luo, B.; Song, R.; Geng, J.; Jing, D.; Zhang, Y. Facile Preparation with High Yield of a 3D Porous Graphitic Carbon Nitride for Dramatically Enhanced Photocatalytic H<sub>2</sub> Evolution under Visible Light. *Appl. Catal. B Environ.* **2018**, *238*, 294–301. [[CrossRef](#)]
86. Ong, W.-J.; Tan, L.-L.; Ng, Y.H.; Yong, S.-T.; Chai, S.-P. Graphitic Carbon Nitride (g-C<sub>3</sub>N<sub>4</sub>)-Based Photocatalysts for Artificial Photosynthesis and Environmental Remediation: Are We a Step Closer to Achieving Sustainability? *Chem. Rev.* **2016**, *116*, 7159–7329. [[CrossRef](#)] [[PubMed](#)]
87. Hisatomi, T.; Takanabe, K.; Domen, K. Photocatalytic Water-Splitting Reaction from Catalytic and Kinetic Perspectives. *Catal. Lett.* **2015**, *145*, 95–108. [[CrossRef](#)]
88. Li, J.; Wu, N. Semiconductor-Based Photocatalysts and Photoelectrochemical Cells for Solar Fuel Generation: A Review. *Catal. Sci. Technol.* **2015**, *5*, 1360–1384. [[CrossRef](#)]
89. Liu, Q.; Chen, T.; Guo, Y.; Zhang, Z.; Fang, X. Ultrathin G-C<sub>3</sub>N<sub>4</sub> Nanosheets Coupled with Carbon Nanodots as 2D/0D Composites for Efficient Photocatalytic H<sub>2</sub> Evolution. *Appl. Catal. B Environ.* **2016**, *193*, 248–258. [[CrossRef](#)]
90. Zhang, J.; Zhang, M.; Yang, C.; Wang, X. Nanospherical Carbon Nitride Frameworks with Sharp Edges Accelerating Charge Collection and Separation at a Soft Photocatalytic Interface. *Adv. Mater.* **2014**, *26*, 4121–4126. [[CrossRef](#)]
91. Lu, L.; Wang, B.; Wang, S.; Shi, Z.; Yan, S.; Zou, Z. La<sub>2</sub>O<sub>3</sub>-Modified LaTiO<sub>2</sub>N Photocatalyst with Spatially Separated Active Sites Achieving Enhanced CO<sub>2</sub> Reduction. *Adv. Funct. Mater.* **2017**, *27*, 1702447. [[CrossRef](#)]
92. Zhu, K.; Lv, Y.; Liu, J.; Wang, W.; Wang, C.; Wang, P.; Meng, A.; Li, Z.; Li, Q. Explosive Thermal Exfoliation of Intercalated Graphitic Carbon Nitride for Enhanced Photocatalytic Degradation Properties. *Ceram. Int.* **2019**, *45*, 3643–3647. [[CrossRef](#)]
93. Cui, Y.; Zhang, J.; Zhang, G.; Huang, J.; Liu, P.; Antonietti, M.; Wang, X. Synthesis of Bulk and Nanoporous Carbon Nitride Polymers from Ammonium Thiocyanate for Photocatalytic Hydrogen Evolution. *J. Mater. Chem.* **2011**, *21*, 13032. [[CrossRef](#)]
94. Chebanenko, M.I.; Zakharova, N.V.; Lobinsky, A.A.; Popkov, V.I. Ultrasonic-Assisted Exfoliation of Graphitic Carbon Nitride and Its Electrocatalytic Performance in Process of Ethanol Reforming. *Semiconductors* **2019**, *53*, 2072–2077. [[CrossRef](#)]
95. Majdoub, M.; Anfar, Z.; Amedlous, A. Emerging Chemical Functionalization of G-C<sub>3</sub>N<sub>4</sub>: Covalent/Noncovalent Modifications and Applications. *ACS Nano* **2020**, *14*, 12390–12469. [[CrossRef](#)] [[PubMed](#)]
96. Hasija, V.; Singh, P.; Thakur, S.; Stando, K.; Nguyen, V.-H.; Le, Q.V.; Alshehri, S.M.; Ahamad, T.; Wu, K.C.-W.; Raizada, P. Oxygen Doping Facilitated N-Vacancies in g-C<sub>3</sub>N<sub>4</sub> Regulates Electronic Band Gap Structure for Trimethoprim and Cr (VI) Mitigation: Simulation Studies and Photocatalytic Degradation Pathways. *Appl. Mater. Today* **2022**, *29*, 101676. [[CrossRef](#)]
97. Yu, H.; Shi, R.; Zhao, Y.; Bian, T.; Zhao, Y.; Zhou, C.; Waterhouse, G.I.N.; Wu, L.; Tung, C.; Zhang, T. Alkali-Assisted Synthesis of Nitrogen Deficient Graphitic Carbon Nitride with Tunable Band Structures for Efficient Visible-Light-Driven Hydrogen Evolution. *Adv. Mater.* **2017**, *29*, 1605148. [[CrossRef](#)] [[PubMed](#)]

98. Xiao, Y.; Tian, G.; Li, W.; Xie, Y.; Jiang, B.; Tian, C.; Zhao, D.; Fu, H. Molecule Self-Assembly Synthesis of Porous Few-Layer Carbon Nitride for Highly Efficient Photoredox Catalysis. *J. Am. Chem. Soc.* **2019**, *141*, 2508–2515. [[CrossRef](#)]
99. Song, X.-L.; Chen, L.; Gao, L.-J.; Ren, J.-T.; Yuan, Z.-Y. Engineering G-C<sub>3</sub>N<sub>4</sub> Based Materials for Advanced Photocatalysis: Recent Advances. *Green Energy Environ.* **2022**, S2468025722001832. [[CrossRef](#)]
100. Ling, G.Z.S.; Oh, V.B.-Y.; Haw, C.Y.; Tan, L.-L.; Ong, W.-J. G-C<sub>3</sub>N<sub>4</sub> Photocatalysts: Utilizing Electron–Hole Pairs for Boosted Redox Capability in Water Splitting. *Energy Mater. Adv.* **2023**, *4*, 0038. [[CrossRef](#)]
101. Rahman, M.Z.; Kwong, C.W.; Davey, K.; Qiao, S.Z. 2D Phosphorene as a Water Splitting Photocatalyst: Fundamentals to Applications. *Energy Environ. Sci.* **2016**, *9*, 709–728. [[CrossRef](#)]
102. Morgan, D.J. Core-Level Reference Spectra for Bulk Graphitic Carbon Nitride (g-C<sub>3</sub>N<sub>4</sub>). *Surf. Sci. Spectra* **2021**, *28*, 014007. [[CrossRef](#)]
103. Ismael, M. Environmental Remediation and Sustainable Energy Generation via Photocatalytic Technology Using Rare Earth Metals Modified G-C<sub>3</sub>N<sub>4</sub>: A Review. *J. Alloys Compd.* **2023**, *931*, 167469. [[CrossRef](#)]
104. Zeng, Y.; Liu, X.; Liu, C.; Wang, L.; Xia, Y.; Zhang, S.; Luo, S.; Pei, Y. Scalable One-Step Production of Porous Oxygen-Doped g-C<sub>3</sub>N<sub>4</sub> Nanorods with Effective Electron Separation for Excellent Visible-Light Photocatalytic Activity. *Appl. Catal. B Environ.* **2018**, *224*, 1–9. [[CrossRef](#)]
105. Lv, C.; Qian, Y.; Yan, C.; Ding, Y.; Liu, Y.; Chen, G.; Yu, G. Defect Engineering Metal-Free Polymeric Carbon Nitride Electrocatalyst for Effective Nitrogen Fixation under Ambient Conditions. *Angew Chem Int Ed* **2018**, *57*, 10246–10250. [[CrossRef](#)] [[PubMed](#)]
106. Wang, Z.; Huang, Y.; Chen, M.; Shi, X.; Zhang, Y.; Cao, J.; Ho, W.; Lee, S.C. Roles of N-Vacancies over Porous g-C<sub>3</sub>N<sub>4</sub> Microtubes during Photocatalytic NO<sub>x</sub> Removal. *ACS Appl. Mater. Interfaces* **2019**, *11*, 10651–10662. [[CrossRef](#)] [[PubMed](#)]
107. Zhang, J.; Xin, B.; Shan, C.; Zhang, W.; Dionysiou, D.D.; Pan, B. Roles of Oxygen-Containing Functional Groups of O-Doped g-C<sub>3</sub>N<sub>4</sub> in Catalytic Ozonation: Quantitative Relationship and First-Principles Investigation. *Appl. Catal. B Environ.* **2021**, *292*, 120155. [[CrossRef](#)]
108. Li, J.; Shen, B.; Hong, Z.; Lin, B.; Gao, B.; Chen, Y. A Facile Approach to Synthesize Novel Oxygen-Doped g-C<sub>3</sub>N<sub>4</sub> with Superior Visible-Light Photoreactivity. *Chem. Commun.* **2012**, *48*, 12017. [[CrossRef](#)]
109. Huang, J.; Nie, G.; Ding, Y. Metal-Free Enhanced Photocatalytic Activation of Dioxygen by g-C<sub>3</sub>N<sub>4</sub> Doped with Abundant Oxygen-Containing Functional Groups for Selective N-Deethylation of Rhodamine B. *Catalysts* **2019**, *10*, 6. [[CrossRef](#)]
110. Ragupathi, V.; Panigrahi, P.; Ganapathi Subramaniam, N. Bandgap Engineering in Graphitic Carbon Nitride: Effect of Precursors. *Optik* **2020**, *202*, 163601. [[CrossRef](#)]
111. Wang, D.; Zhang, Z.; Xu, S.; Guo, Y.; Kang, S.; Chang, X. H<sub>2</sub>+CO<sub>2</sub> Synergistic Plasma Positioning Carboxyl Defects in G-C<sub>3</sub>N<sub>4</sub> with Engineered Electronic Structure and Active Sites for Efficient Photocatalytic H<sub>2</sub> Evolution. *Int. J. Mol. Sci.* **2022**, *23*, 7381. [[CrossRef](#)]
112. Li, Y.; Li, X.; Zhang, H.; Fan, J.; Xiang, Q. Design and Application of Active Sites in G-C<sub>3</sub>N<sub>4</sub>-Based Photocatalysts. *J. Mater. Sci. Technol.* **2020**, *56*, 69–88. [[CrossRef](#)]
113. She, X.; Liu, L.; Ji, H.; Mo, Z.; Li, Y.; Huang, L.; Du, D.; Xu, H.; Li, H. Template-Free Synthesis of 2D Porous Ultrathin Nonmetal-Doped g-C<sub>3</sub>N<sub>4</sub> Nanosheets with Highly Efficient Photocatalytic H<sub>2</sub> Evolution from Water under Visible Light. *Appl. Catal. B Environ.* **2016**, *187*, 144–153. [[CrossRef](#)]
114. Zhu, X.; Duan, C.; Wang, W.; Xin, G.; Song, J. Fabrication of Carboxylated G-C<sub>3</sub>N<sub>4</sub> with Excellent Adsorption and Photocatalytic Properties. *Mater. Lett.* **2022**, *317*, 132045. [[CrossRef](#)]
115. Sharma, R.; Almáši, M.; Nehra, S.P.; Rao, V.S.; Panchal, P.; Paul, D.R.; Jain, I.P.; Sharma, A. Photocatalytic Hydrogen Production Using Graphitic Carbon Nitride (GCN): A Precise Review. *Renew. Sustain. Energy Rev.* **2022**, *168*, 112776. [[CrossRef](#)]
116. Rahman, M.Z.; Davey, K.; Mullins, C.B. Tuning the Intrinsic Properties of Carbon Nitride for High Quantum Yield Photocatalytic Hydrogen Production. *Adv. Sci.* **2018**, *5*, 1800820. [[CrossRef](#)] [[PubMed](#)]
117. Tan, M.; Yu, C.; Li, J.; Li, Y.; Tao, C.; Liu, C.; Meng, H.; Su, Y.; Qiao, L.; Bai, Y. Engineering of G-C<sub>3</sub>N<sub>4</sub>-Based Photocatalysts to Enhance Hydrogen Evolution. *Adv. Colloid Interface Sci.* **2021**, *295*, 102488. [[CrossRef](#)] [[PubMed](#)]
118. Sun, N.; Liang, Y.; Ma, X.; Chen, F. Reduced Oxygenated g-C<sub>3</sub>N<sub>4</sub> with Abundant Nitrogen Vacancies for Visible-Light Photocatalytic Applications. *Chem. A Eur. J* **2017**, *23*, 15466–15473. [[CrossRef](#)] [[PubMed](#)]
119. Xue, Y.; Ma, C.; Yang, Q.; Wang, X.; An, S.; Zhang, X.; Tian, J. Construction of G-C<sub>3</sub>N<sub>4</sub> with Three Coordinated Nitrogen (N<sub>3</sub>C) Vacancies for Excellent Photocatalytic Activities of N<sub>2</sub> Fixation and H<sub>2</sub>O<sub>2</sub> Production. *Chem. Eng. J.* **2023**, *457*, 141146. [[CrossRef](#)]
120. Wang, L.; Li, F.; He, Q.; Liu, X.; Yu, C. Fabrication of Nitrogen-Deficient g-C<sub>3</sub>N<sub>4</sub> Nanosheets via an Acetaldehyde-Assisted Hydrothermal Route and Their High Photocatalytic Performance for H<sub>2</sub>O<sub>2</sub> Production and Cr(vi) Reduction. *New J. Chem.* **2023**, *47*, 12595–12607. [[CrossRef](#)]
121. Jiang, X.; Liu, Y.; Wang, T.; Xia, B.; Qian, J.; Ran, J.; Zhang, Z.; Gao, D. High-Temperature Ferromagnetism in Non-Metal Carbonitride: From Nitrogen Vacant g-C<sub>3</sub>N<sub>4</sub> to N-Doped Graphene. *J. Magn. Magn. Mater.* **2021**, *538*, 168223. [[CrossRef](#)]
122. Coleman, J.N.; Lotya, M.; O'Neill, A.; Bergin, S.D.; King, P.J.; Khan, U.; Young, K.; Gaucher, A.; De, S.; Smith, R.J.; et al. Two-Dimensional Nanosheets Produced by Liquid Exfoliation of Layered Materials. *Science* **2011**, *331*, 568–571. [[CrossRef](#)] [[PubMed](#)]
123. Hernandez, Y.; Nicolosi, V.; Lotya, M.; Blighe, F.M.; Sun, Z.; De, S.; McGovern, I.T.; Holland, B.; Byrne, M.; Gun'Ko, Y.K.; et al. High-Yield Production of Graphene by Liquid-Phase Exfoliation of Graphite. *Nat. Nanotech* **2008**, *3*, 563–568. [[CrossRef](#)] [[PubMed](#)]

124. Yang, S.; Gong, Y.; Zhang, J.; Zhan, L.; Ma, L.; Fang, Z.; Vajtai, R.; Wang, X.; Ajayan, P.M. Exfoliated Graphitic Carbon Nitride Nanosheets as Efficient Catalysts for Hydrogen Evolution Under Visible Light. *Adv. Mater.* **2013**, *25*, 2452–2456. [[CrossRef](#)] [[PubMed](#)]
125. Luo, Y.; Zhu, Y.; Han, Y.; Ye, H.; Liu, R.; Lan, Y.; Xue, M.; Xie, X.; Yu, S.; Zhang, L.; et al. G-C<sub>3</sub>N<sub>4</sub>-Based Photocatalysts for Organic Pollutant Removal: A Critical Review. *Carbon Res.* **2023**, *2*, 14. [[CrossRef](#)]
126. García-Mulero, A.; Rendón-Patiño, A.; Asiri, A.M.; Primo, A.; Garcia, H. Band Engineering of Semiconducting Microporous Graphitic Carbons by Phosphorous Doping: Enhancing of Photocatalytic Overall Water Splitting. *ACS Appl. Mater. Interfaces* **2021**, *13*, 48753–48763. [[CrossRef](#)] [[PubMed](#)]
127. Kong, L.; Wang, J.; Mu, X.; Li, R.; Li, X.; Fan, X.; Song, P.; Ma, F.; Sun, M. Porous Size Dependent G-C<sub>3</sub>N<sub>4</sub> for Efficient Photocatalysts: Regulation Synthesizes and Physical Mechanism. *Mater. Today Energy* **2019**, *13*, 11–21. [[CrossRef](#)]
128. Cui, L.; Liu, Y.; Wang, Y.; Fang, X.; Yin, C.; Kang, S.; Dong, M. Constructing Ultrathin G-C<sub>3</sub>N<sub>4</sub> Nanosheets with Hierarchical Pores by NaClO Induced Wet Etching for Efficient Photocatalytic Cr(VI) Detoxification under Visible Light Irradiation. *Diam. Relat. Mater.* **2018**, *88*, 51–59. [[CrossRef](#)]
129. Wen, J.; Xie, J.; Chen, X.; Li, X. A Review on G-C<sub>3</sub>N<sub>4</sub>-Based Photocatalysts. *Appl. Surf. Sci.* **2017**, *391*, 72–123. [[CrossRef](#)]
130. Zhang, S.; Gu, P.; Ma, R.; Luo, C.; Wen, T.; Zhao, G.; Cheng, W.; Wang, X. Recent Developments in Fabrication and Structure Regulation of Visible-Light-Driven g-C<sub>3</sub>N<sub>4</sub>-Based Photocatalysts towards Water Purification: A Critical Review. *Catal. Today* **2019**, *335*, 65–77. [[CrossRef](#)]
131. Long, B.; Yan, G.; He, H.; Meng, S. Porous and Few-Layer Carbon Nitride Nanosheets via Surface Steam Etching for Enhanced Photodegradation Activity. *ACS Appl. Nano Mater.* **2022**, *5*, 7798–7810. [[CrossRef](#)]
132. Xu, R.; Li, J.; Sui, G.; Zhuang, Y.; Guo, D.; Luo, Z.; Liang, S.; Yao, H.; Wang, C.; Chen, S. Constructing Supramolecular Self-Assembled Porous g-C<sub>3</sub>N<sub>4</sub> Nanosheets Containing Thiophene-Groups for Excellent Photocatalytic Performance under Visible Light. *Appl. Surf. Sci.* **2022**, *578*, 152064. [[CrossRef](#)]
133. Zhang, Q.; Yang, F.; Zhou, S.; Bao, N.; Xu, Z.; Chaker, M.; Ma, D. Broadband Photocatalysts Enabled by 0D/2D Heterojunctions of near-Infrared Quantum Dots/Graphitic Carbon Nitride Nanosheets. *Appl. Catal. B Environ.* **2020**, *270*, 118879. [[CrossRef](#)]
134. Zhang, X.; Jia, X.; Duan, P.; Xia, R.; Zhang, N.; Cheng, B.; Wang, Z.; Zhang, Y. V<sub>2</sub>O<sub>5</sub>/P-g-C<sub>3</sub>N<sub>4</sub> Z-Scheme Enhanced Heterogeneous Photocatalytic Removal of Methyl Orange from Water under Visible Light Irradiation. *Colloids Surf. A Physicochem. Eng. Asp.* **2021**, *608*, 125580. [[CrossRef](#)]
135. Kampalapura Swamy, C.; Hezam, A.; Mavinakere Ramesh, A.; Habbanakuppe Ramakrishnegowda, D.; Purushothama, D.K.; Krishnegowda, J.; Kanchugarakoppal S., R.; Shivanna, S. Microwave Hydrothermal Synthesis of Copper Induced ZnO/gC<sub>3</sub>N<sub>4</sub> Heterostructure with Efficient Photocatalytic Degradation through S-Scheme Mechanism. *J. Photochem. Photobiol. A Chem.* **2021**, *418*, 113394. [[CrossRef](#)]
136. Liu, R.; Yang, W.; He, G.; Zheng, W.; Li, M.; Tao, W.; Tian, M. Ag-Modified g-C<sub>3</sub>N<sub>4</sub> Prepared by a One-Step Calcination Method for Enhanced Catalytic Efficiency and Stability. *ACS Omega* **2020**, *5*, 19615–19624. [[CrossRef](#)] [[PubMed](#)]
137. Dou, Q.; Hou, J.; Hussain, A.; Zhang, G.; Zhang, Y.; Luo, M.; Wang, X.; Cao, C. One-Pot Synthesis of Sodium-Doped Willow-Shaped Graphitic Carbon Nitride for Improved Photocatalytic Activity under Visible-Light Irradiation. *J. Colloid Interface Sci.* **2022**, *624*, 79–87. [[CrossRef](#)]
138. Liu, F.; Nguyen, T.-P.; Wang, Q.; Massuyeau, F.; Dan, Y.; Jiang, L. Construction of Z-Scheme g-C<sub>3</sub>N<sub>4</sub>/Ag/P3HT Heterojunction for Enhanced Visible-Light Photocatalytic Degradation of Tetracycline (TC) and Methyl Orange (MO). *Appl. Surf. Sci.* **2019**, *496*, 143653. [[CrossRef](#)]
139. Huang, Z.; Jia, S.; Wei, J.; Shao, Z. A Visible Light Active, Carbon–Nitrogen–Sulfur Co-Doped TiO<sub>2</sub>/g-C<sub>3</sub>N<sub>4</sub> Z-Scheme Heterojunction as an Effective Photocatalyst to Remove Dye Pollutants. *RSC Adv.* **2021**, *11*, 16747–16754. [[CrossRef](#)]
140. Santha kumar, K.; Vellaichamy, B.; Paulmony, T. Visible Light Active Metal-Free Photocatalysis: N-Doped Graphene Covalently Grafted with g-C<sub>3</sub>N<sub>4</sub> for Highly Robust Degradation of Methyl Orange. *Solid State Sci.* **2019**, *94*, 99–105. [[CrossRef](#)]
141. G-C<sub>3</sub>N<sub>4</sub> Quantum Dot Decorated MoS<sub>2</sub>/Fe<sub>3</sub>O<sub>4</sub> as a Novel Recoverable Catalyst for Photodegradation of Organic Pollutant under Visible Light | Journal of Materials Science: Materials in Electronics. Available online: <https://link.springer.com/article/10.1007/s10854-021-06790-w> (accessed on 29 November 2023).

**Disclaimer/Publisher’s Note:** The statements, opinions and data contained in all publications are solely those of the individual author(s) and contributor(s) and not of MDPI and/or the editor(s). MDPI and/or the editor(s) disclaim responsibility for any injury to people or property resulting from any ideas, methods, instructions or products referred to in the content.